Journal of Structural Geology 33 (2011) 1265–1284

Contents lists available at ScienceDirect

Journal of Structural Geology

journal homepage: www.elsevier.com/locate/jsg

Quartz grain size reduction in a granitoid rock and the transition from dislocation to diffusion creep

Rüdiger Kilian [a,*], Renée Heilbronner [a], Holger Stünitz [b]

[a] Geological Institute, Department of Environmental Sciences, Basel University, Bernoullistrasse 32, CH-4056 Basel, Switzerland
[b] Department of Geology, University of Tromsø, Dramsveien 201, 9037 Tromsø, Norway

ARTICLE INFO

Article history:
Received 29 September 2010
Received in revised form
11 May 2011
Accepted 14 May 2011
Available online 25 May 2011

Keywords:
Dislocation creep
Diffusion creep
Polymineralic rheology
Grain size reduction
Cavitation
Pinning
Dissolution–precipitation
Phase boundary migration
Dynamic recrystallization

ABSTRACT

In the Gran Paradiso metagranodiorite (Western Alps) small scale lower amphibolite facies shear zones record the transition from a mylonite composed of polycrystalline mineral aggregates to a homogeneous ultramylonite with a grain scale phase mixture. Polycrystalline quartz aggregates in the mylonite deform by dislocation creep developing a crystallographic preferred orientation (CPO) and a monoclinic surface orientation distribution function (ODF). The polymineralic matrix of the mylonite and the ultramylonite deform by diffusion creep. In the ultramylonite the quartz CPO is randomized and the surface ODF becomes orthorhombic. The transition from mylonite to ultramylonite is accompanied by a grain size decrease and a disintegration of quartz aggregates, concomitant with the precipitation of K-feldspar (±biotite) between quartz grains.

In quartz, reduction from the dynamically recrystallized grain size in the aggregates (110 μm) to the size of the dispersed grains in the ultramylonite (25 μm) occurs through the following processes: K-feldspar precipitates at opening sites along grain boundaries (strain incompatibility) pinning the grain size in quartz aggregates. Coalescence of K-feldspar leads to enhanced grain boundary sliding and disintegration of the quartz aggregates. Solution precipitation reduces the size of the dispersed grains to less than subgrain size (~45 μm).

1. Introduction

High strain viscous deformation in natural shear zones frequently produces two types of microstructures: (1) Monomineralic aggregates and (2) Polymineralic mixtures. Both microstructures may occur in the same shear zone in alternating layers. The monomineralic layers typically deform by dislocation creep as indicated by a strong crystallographic preferred orientation (CPO; e.g. Baker and Wenk, 1972), a strong shape preferred orientation (SPO; Schmid et al., 1987; Stipp et al., 2002), and by characteristic dynamic recrystallization microstructures (e.g. Hirth and Tullis, 1992; Stipp et al., 2002).

The polymineralic mixtures are often characterized by a fine grain size and a high degree of mixing of phases. Many workers agree that the latter two properties are an expression of diffusion creep with grain boundary sliding (e.g. Boullier and Gueguen, 1975; Stünitz and Fitz Gerald, 1993; Fliervoet et al., 1997; Kruse and Stünitz, 1999; Mehl and Hirth, 2008; Kanagawa et al., 2008). Diffusion creep is further indicated by a weakening of the crystallographic preferred orientation (CPO) (e.g. Edington et al., 1976; Schmid, 1982; Behrmann and Mainprice, 1987; Song and Ree, 2007) and characteristic grain boundary geometry and alignment (Drury and Humphreys, 1988).

A potential switch from dislocation creep to diffusion creep is characterized by grain size reduction. The most common processes for grain size reduction are dynamic recrystallization (Schmid, 1982; Behrmann, 1985; Fliervoet and White, 1995), neomineralization/mineral reactions (Kerrich et al., 1980; Rubie, 1983; Fitz Gerald and Stünitz, 1993; Stünitz and Fitz Gerald, 1993, De Ronde et al., 2005) and nucleation and growth of new grains with a different composition (Kruse and Stünitz, 1999; Kenkmann and Dresen, 2002). A small grain size can be retained due to impeded grain growth in the phase mixture.

The transition from dislocation to diffusion dominated creep has great consequences for the rheological behavior of the rock. Thus, the questions of what triggers or controls such a transition and which processes are active are essential to understand viscous rock deformation. In order to analyze these aspects, we present a detailed microstructural study on small scale shear zones in a metagranodiorite covering the progressive transition from a mylonite

* Corresponding author. Tel.: +41 61 2673607.
E-mail address: ruediger.kilian@unibas.ch (R. Kilian).

0191-8141/$ – see front matter © 2011 Elsevier Ltd. All rights reserved.
doi:10.1016/j.jsg.2011.05.004

with monophase polycrystalline quartz aggregates embedded in a polymineralic matrix to an ultramylonitic phase mixture. The main points of the paper will be to discuss the microstructural transition and the associated processes which explain the quartz grain size reduction, phase mixing, and CPO destruction. The complete microstructural development of the mylonite from the protolith is beyond the scope of this contribution.

In the analyzed shear zone quartz constitutes the rheologically stronger phase which does not appear to be atypical in many natural shear zones. However quartz is often considered (by experimentalists, theoreticians, and modelers) as weak mineral and therefore key mineral to estimate crustal strength (e.g. Kohlstedt et al., 1995 and references therein).

2. Geological setting and sample description

The samples investigated are from three small-scale shear zones in the metagranodiorite of the Gran Paradiso Unit from of the Gran Paradiso nappe in the Piantonetto valley (Alpe Drosa area and Lago Teleccio area; GP4: 32T0371554/5037041,GP9: 32T372881/5038395 GP11: 32T0371389/5037047). These rocks have been studied intensively (mainly by LeGoff and Ballevre, 1990; Brouwer et al., 2002; Menegon et al., 2006, 2008; Menegon and Pennacchioni, 2010). The intrusives are heterogeneously deformed during the Alpine orogeny (e.g. Le Bayon et al., 2006) and preserve meter to kilometer scale low strain domains surrounded by granitic orthogneisses (Callegari et al., 1969). The low strain domains host the studied small-scale shear zones which are coeval with the main deformation of the Gran Paradiso nappe (Menegon and Pennacchioni, 2010).

The granitoids underwent an early, at least in the low strain domains, static high-pressure metamorphism at around 1.0–1.6 GPa and 500–550 °C. During the later formation of the shear zones, the pressure decreased to 0.6–0.7 GPa while the temperature remained relatively high at 550 ± 50 °C (LeGoff and Ballevre, 1990; Brouwer et al., 2002).

The shear zones are straight, regularly spaced, subparallel, up to several centimeters wide, and planar over distances up to several tens of meters (Menegon, 2006; Menegon and Pennacchioni, 2010). Samples display a strain gradient from weakly deformed metagranodiorite (protolith) to mylonites to fine-grained ultramylonites (Fig. 1). The transition from mylonite to ultramylonite – near the center of the shear zone occurs over a few mm and can be observed within a single thin section (Figs. 2 and 3).

In the studied metagranodiorite we distinguish a protolith, a mylonite and an ultramylonite with a transition zone. The protolith is a metagranodiorite and occasionally shows a weak initial foliation defined by the preferred elongation and orientation of aggregates of polycrystalline plagioclase and biotite. K-feldspar crystals (up to 15 mm long) display a weak alignment. Quartz grains of magmatic origin are up to several mm in diameter; in the close vicinity of relatively rigid K-feldspar porphyroclasts, they may recrystallize dynamically along the grain

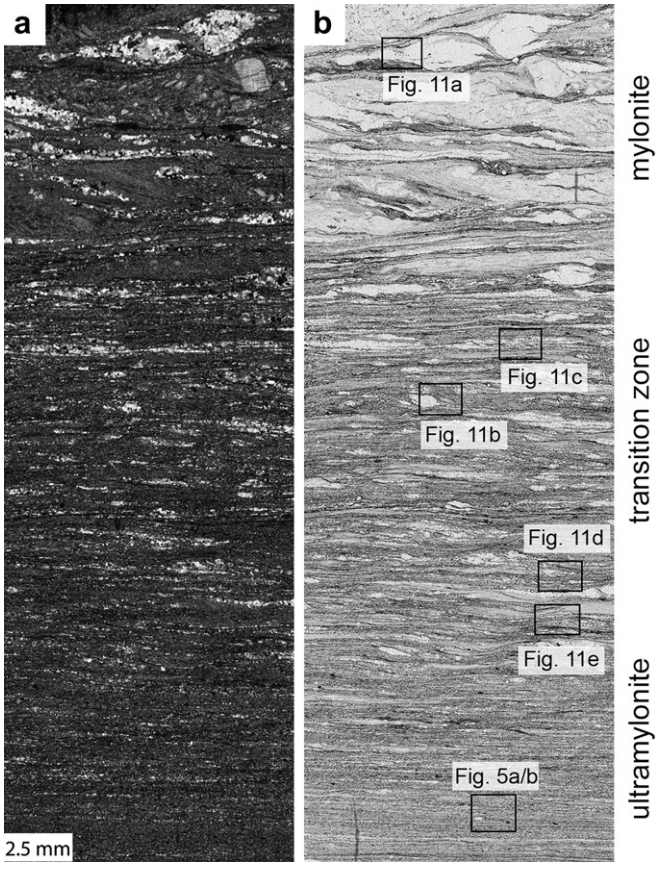

Fig. 2. Micrograph of the central part of a sinistral shear zone (scans of thin section, crossed polarizers/plane light). The mylonitic part of the shear zone contains aggregates of recrystallized quartz, a K-felspar porphyroclast, and the fine-grained polymineralic matrix. In the transition zone, quartz aggregates are progressively disintegrated. In the center of the shear zone, the ultramylonite consists of homogeneously mixed phases and polycrystalline quartz aggregates have entirely disappeared (sample GP4-3).

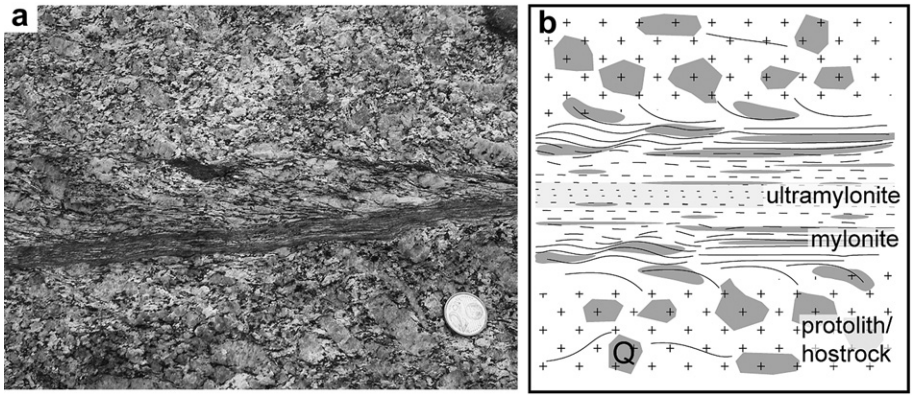

Fig. 1. (a) Field view of a small-scale sinistral shear zone in the Gran Paradiso metagranodiorite, similar to the sampled shear zones. The coin measures 19 mm. (b) Sketch of a shear zone in the Gran Paradiso metagranodiorite. Quartz aggregates (Q) deform in a polymineralic matrix.

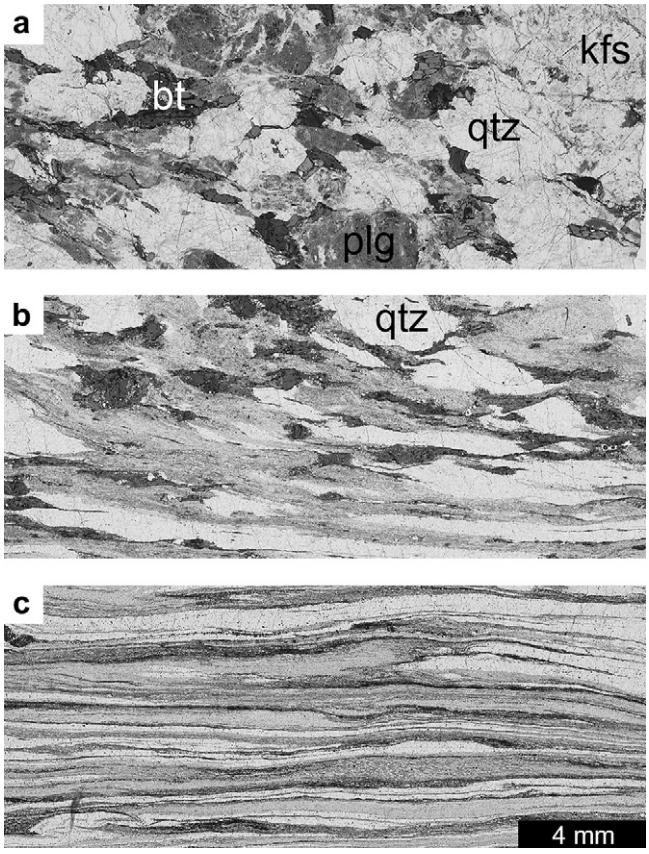

Fig. 3. Sequence of weakly deformed historic, shear zone margin and highly deformed, mylonitic granodiorite. Quartz aggregates form elongate lenses embedded in the matrix. In the high strain part of the mylonite, layers of recrystallized quartz and matrix are parallel to the shear zone zone boundary. Scans of thin sections, plane light. qtz: quartz, kfs: k-feldspar, plg: plagioclase, bt: biotite.

margins (Fig. 3). In the protolith polycrystalline plagioclase aggregates statically replace magmatic plagioclase as a result of the high-pressure metamorphism.

In the mylonitic part, the K-feldspar clasts and the biotite are dynamically recrystallized (Menegon et al., 2006). Together with the plagioclase aggregates they form interconnected layers of varying composition and variable degree of mixing. The magmatic quartz grains are also completely recrystallized and form polycrystalline aggregates. They appear as more viscous domains in the fine-grained matrix of K-feldspar, biotite and plagioclase. With increasing deformation, the quartz aggregates elongate until they form continuous layers which can diminish to a thickness of a single grain (Fig. 3). As deformation progresses quartz aggregates and layers are converted to quartz-K-feldspar layers.

In the ultramylonite, the quartz layers are disintegrated and mixed into the surrounding matrix. At that point no layering can be observed anymore, all phases are thoroughly mixed. During the disintegration of the quartz aggregates and continued deformation the quartz grain size decreases until all phases have approximately the same grain size in the center of the shear zone (Fig. 2).

In the following, the shear zones will be displayed such that on all micrographs the shear sense is sinistral (except Fig. 14). The shear zone boundaries are horizontal (parallel to the X–Y plane), the transport direction is X, the shear zone normal is Z and the transverse direction, assumed to be the vorticity axis, is Y. The positive *X*-axis is 0°, angles are measured counterclockwise. The foliation is defined by a compositional layering or aligned grains, its overall orientation varies from a dip of approximately −15 to −45° (for sinistral shear sense) in the mylonite to effectively 0° in the ultramylonite. Locally, in particular around quartz aggregates in the mylonite, deviations may occur. An offset along one of the shear zones studied here, was measured to be 0.4 m, producing a local shear strain, γ, of 40. This value is a typical value for sample GP11. For samples GP4 and GP9 it is assumed to be much higher.

3. Analytical methods

3.1. Texture analysis and orientation imaging

We used EBSD for the texture analysis. Using a ZEISS Evo 50 SEM equipped with a Digiview II EBSD camera and OIM® acquisition software, the Euler angles were measured. Samples were polished and lapped with SYTON-fluid (Fynn and Powell, 1979). The polishing procedure was optimized for quartz to ensure that we got good quality EBSPs for quartz. At the same time, the feldspars etched more rapidly and produced a negative relief. The pattern quality of K-feldspar and plagioclase were generally not good enough for reliable indexing. EBSP were obtained at step sizes between 1 and 6.75 μm. During EBSP acquisition, element maps were recorded by energy dispersive spectroscopy (EDS); they were used for the calculation of phase maps and masks that would block all non-quartz-phases from the analysis.

For better visualization the Euler angle images were transformed to *c*-axis orientation images.

In addition three principal misorientation images were calculated using the CIP (computer integrated polarization microscopy) software, which served as the basis for image segmentation and grain size determination.

Pole figures were calculated using the MTEX software (Hielscher and Schaeben, 2008) from the raw EBSD output. To evaluate the effect of grain-size-dependent CPOs, grains were segmented at 7.5° misorientation (using OIM® software) and CPOs calculated for different grain size bins using both the average orientation and the area-weighted average orientation of the grain. In the case of OIM® calculated grain data, many grains consisted of only few pixels. However, only grains larger 9 square pixels were considered as grains to omit artefacts from single-measurement grains introduced by the OIM® software cleanup routine.

The maximum of a pole figure depends on the kernel width, the CPO geometry, and on the number of individual grains that have been measured and only yields a rough estimate of the strength of a CPO. If the full ODF is known, the M-index can be calculated. It is proposed as a robust description of a texture strength omitting the problems associated with the examination of pole figure maxima (Skemer et al., 2005).

3.2. Grain size analysis

Grain sizes were measured from grain maps. Two types of source images were used: SEM/BSE contrast images and the three principal misorientation images. Grain maps were obtained by supervised segmentation using the freeware Image SXM (http://www.ImageSXM.org.uk) and the Lazy grain boundaries macro (http://pages.unibas.ch/earth/micro).

On the grain maps, the cross sectional areas were measured and the equivalent diameters, $\mathrm{dequ} = 2\cdot\sqrt{(\mathrm{area}/\pi)}$, were calculated. Number-weighted histograms, $h(\mathrm{dequ})$, were used as input for the STRIPSTAR (Heilbronner and Bruhn, 1998) program and number-weighted $h(D)$ and volume weighted histograms, $V(D)$, of the diameters, D, of the calculated volume equivalent spheres were derived. Using a sample size of 120–4500, the percentage of anti-spheres remained below 1% and hence the derived 3D grain size distributions were considered valid. For both distributions of

spheres average grain sizes were calculated: the number-weighted mean $\mu_N = \sum(hi(Di)\cdot Di)$ and the volume weighted mean, $\mu_V = \sum(Vi(Di)\cdot Di)$ assuming that $\sum Vi(Di) = 1.00$ and $\sum hi(Di) = 1.00$. The number-weighted mean of 2-dimensional distributions is termed μ_n.

3.3. Microstructure analysis

Using subsets of the best resolved grains from the grain maps used for grain size analysis up to ~200 grains were selected. The particle fabric is quantified using the PAROR method (Panozzo, 1983) and the surface fabric by the SURFOR method (Panozzo, 1984). The preferred orientation of particles and of grain surfaces are presented as orientation distribution functions (ODF, i.e., length weighted rose diagrams) of long axes and surface elements. The axial ratio of each grain, b/a, is determined by the ratio of the projection normal to the longest divided by the longest projection, axperp./axlong. The average axial ratio of the grains is the mean of the individual axial ratios, b/a, of all the grains.

The bulk properties of the particle fabric as a whole are determined from the projection curves $B(\alpha)$ and $A(\alpha)$. The bulk axial ratio, (b/a)bulk, is determined by the ratio of the minimum to the maximum of the projection curves $B(\alpha)$: $B(\alpha)\text{min}/B(\alpha)\text{max} = b/a$. The bulk preferred orientation of grains is obtained from the angle (αmin) at the minimum of $B(\alpha)$: $\alpha p = 90^\circ - \alpha\text{min}$ (Panozzo, 1984). The ratio (b/a)bulk is different from the arithmetic mean of axial ratios of the individual grains since it does not only depend on the axial ratio of the grains but also on the orientation of the grains with respect to one another.

The shape of the individual grains, i.e., the lobateness of the grain boundaries, is described in terms of the PARIS factor (Panozzo and Hurlimann, 1983). The length of the actual perimeter is compared to the perimeter of the convex hull: $\text{PARIS} = 2 \times (\text{P} - \text{PE})/\text{PE}$, where P is the perimeter and PE the perimeter of the convex hull (Heilbronner and Keulen, 2006). For a given fabric, the numerical average of the PARIS factors of the grains is calculated.

The sources for CIP, STRIPSTAR, SURFOR, PAROR and ISHAPES, the software which calculates the PARIS factor, are available at http://pages.unibas.ch/earth/micro.

3.4. Quartz distribution analysis

Phase distribution analysis was used previously to test the randomness of mixtures using the method of Kretz (1969). A two-phase mixture of equi-sized grains can be tested for clustering, randomness or anticlustering by a comparison of phase and grain boundary fractions at different volume proportions with the theoretically predicted distributions (Mackenzie et al., 2008). Because of changing grain sizes Kretz's method cannot be used. Instead we use the relative frequency of grain boundary and phase boundary contacts of quartz. We measured the total length, Lg, of the quartz–quartz grain boundary and the total length, Lp of the quartz–matrix phase boundary. The ratio, Rgp is calculated as Lg/Lp. The lower the Rgp the more intensive is the mixing of quartz within the matrix phases.

3.5. Modal content of quartz

Modal content was determined from SEM/BSE images, from phase maps that were calculated from EDS element counts, or from transmitted-light light photomicrographs.

The quartz content was measured at different scales. In the weakly deformed to mylonitic part of the shear zone, the composition is homogeneous only in areas of a few cm^2, in ultramylonites, the quartz content could be derived on much smaller areas (<1 mm^2).

4. Results

The mylonitic metagranodiorite appears as a rheologically bi-phase material consisting of (1) polycrystalline quartz aggregates and K-feldspar porphyroclasts (both of slightly higher viscosity) embedded in (2) a polymineralic matrix of lower viscosity (Figs. 2 and 3). Rheologically bi-phase material is a rough approximation and we distinguish between a rheological phase and a mineralogical phase. The ultramylonite consists of a homogeneous mixture of quartz and the former matrix phases and is considered as rheologically monophase (above the grain scale) (Fig. 2).

The results will be presented in the following sequence: The first section will concern quartz in the mylonite and the ultramylonite. The second section will concern all the other major minerals constituting the matrix in the mylonite and the ultramylonite (except quartz). The third section concerns the microstructural transition from the mylonite to the ultramylonite. The evolution of the quartz distribution will be treated in the last section.

4.1. Quartz

The quartz aggregates are fully recrystallized and appear as elongate objects with a size corresponding to the magmatic grain size ($d \sim 3$–6 mm) and closely aligned with the foliation. In the most highly strained parts of the mylonite they are elongate lenses and, finally, very thin layers parallel to the flow plane of the shear zone (Figs. 3 and 4a). At a certain point, the aggregates become so long that their areas cannot be measured in a single thin section (Fig. 3). The width of the layers can decrease to a thickness of a single grain. In the most highly strained parts of the mylonites, the layers begin to disintegrate (Fig. 2).

Recrystallized quartz grains in the mylonite have a slightly lobate shape and boundaries are occasionally pinned at second phase particles (Fig. 4b), though most grain boundaries are composed of straight surface elements.

The ultramylonite consists of a phase mixture where a distinction between quartz aggregates and matrix is impossible (Fig. 5). Quartz grains are completely dispersed among the other matrix phases. The remaining quartz–quartz grain boundaries are rather smooth corresponding to those observed in the monomineralic quartz aggregates in the mylonite (Figs. 4 and 5). Quartz–plagioclase phase boundaries are slightly lobate and show micron-scale bulges while quartz-K-feldspar boundaries are often broadly curved (Fig. 5b).

4.1.1. Grain sizes

The diameter of the recrystallized quartz grains in the mylonite ranges between 40 and 200 μm; with $\mu_V = 110$ μm (Fig. 6a). The mean grain size does not change with increasing finite strain or aspect ratio of the aggregate. The quartz grain size in the ultramylonite is reduced to a μ_V of 62 μm and the very finest fraction in the shear zone has a μ_V of 23 μm (Fig. 6b,c).

Subgrain boundaries in the recrystallized grains recorded by EBSD and CIP are infrequent. Most subgrain boundaries $<7.5^\circ$ cut across larger grains and the resulting "cells" are within the lower range of size distribution of recrystallized grains (20–65 μm eq. diameter, Fig. 6d).

4.1.2. Quantitative microstructures

The PAROR analysis of the recrystallized grains yields a bulk axial ratio, (b/a)bulk of ~0.8, and an average axial ratio, b/a, of the grains of ~0.6. Thus, there is a weak but consistent shape preferred orientation (Fig. 6e) with a preferred orientation of particle long axes inclined at approx. 125°–145°, i.e., inclined with the sense of shear. The ODF of grain surfaces shows an internal monoclinic

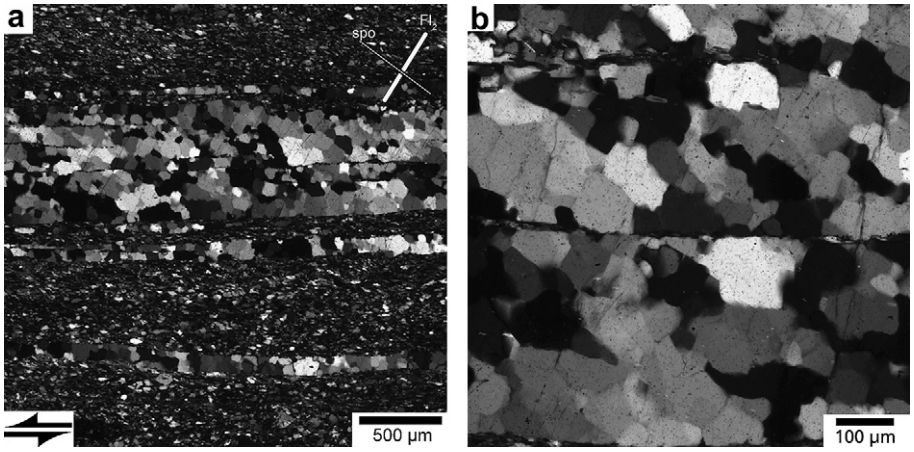

Fig. 4. Quartz microstructures. (a) Stretched quartz aggregates embedded in the polymineralic matrix. Cross-polarized light. Note weak oblique grain shape preferred orientation indicating sinistral shear sense. Fluid inclusion trails and cracks are oriented at right angles (FI). Horizontal discontinuities inside the quartz layers are mostly K-feldspar seams and minor biotite flakes. (b) Detail of quartz microstructure (cross-polarized light).

symmetry. The first maximum is at 160° and the second one at 95°. At higher strains, some quartz aggregates show diamond-shaped grain junctions (Drury and Humphreys, 1988).

The quartz grains in the ultramylonite have an equant shape with bulk axial ratios, b/a of >0.89 (Fig. 6f). Surface ODFs show that boundaries are preferentially oriented parallel and normal to the foliation (Fig. 6f) implying a square to rectangular shape (compare Fig. 5b). In the more mica-rich domains, some of the long axes of grains are aligned parallel to the foliation.

From the mylonite to the ultramylonite, the PARIS factor of the quartz grains decreases from an average of ~10%–~4%. (Fig. 6g). This is consistent with straighter grain boundaries, more rounded corners and less concave grain boundary embayments in the ultramylonite.

4.1.3. Crystallographic preferred orientation

Quartz aggregates in the mylonite show a CPO with a strong peripheral *c*-axis maximum between 95 and 110° to the foliation rotated synthetically with the sense of shear (Fig. 7a,b). A weak single girdle is developed and in some aggregates a minor maximum parallel to Y occurs. The <a> axes form a maximum close to the lineation. Subgrain boundaries are usually found in the partly recrystallized aggregates of the low strain parts of the shear zones but only rarely in recrystallized grains. In most cases, they are parallel to the traces of the {10–10} prism planes. The M-index in the quartz aggregates is ~0.5 (Fig. 7c).

The typical inclined, peripheral *c*-axis maximum of the mylonite disappears in the ultramylonite (Fig. 10) and the intensity of the CPO, as indicated by the maximum of the pole figure, is much lower than in the mylonite (Fig. 7d,e). In the ultramylonite quartz grains are generally free of optical subgrains and do not show undulatory extinction. EBSD derived orientation maps rarely show subgrain boundaries (<7.5°) which are almost exclusively parallel to the traces of the *c*-axes. The M-index decreases to <0.05 in the dispersed grains of the ultramylonite (Fig. 7f).

4.1.4. Volume fraction

The modal content of quartz does not change from the mylonite to the ultramylonite (Fig. 8). At first the quartz is concentrated in the quartz aggregates. Progressive disintegration of the quartz

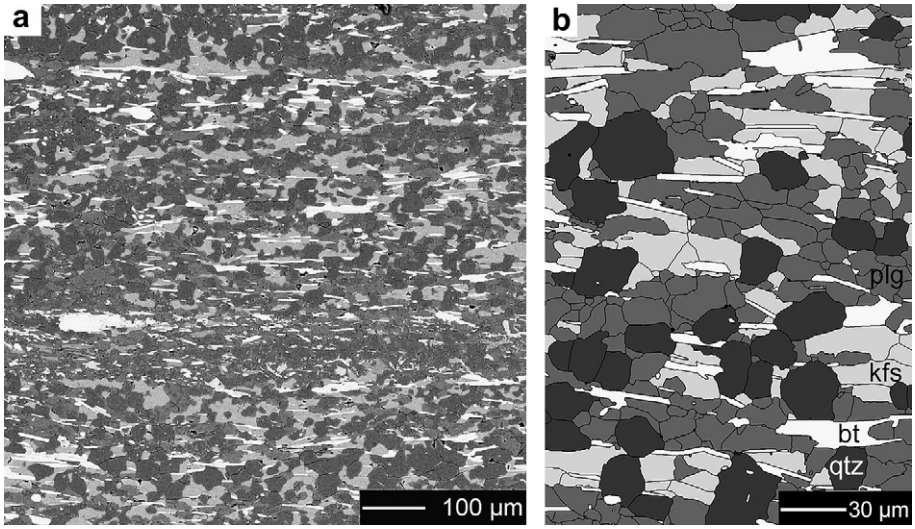

Fig. 5. Microstructure of the ultramylonite. (a) SEM/BSE image of the homogenous phase mixture with the 30% quartz formerly contained in the polycrystalline quartz aggregates. (b) Drawing of a microstructure in the ultramylonite, detail of a). Quartz is dark, oligoclase is medium-grey, K-feldspar is light grey and biotite is white. For location see Fig. 2. qtz: quartz, kfs: K-feldspar, plg: plagioclase, bt: biotite.

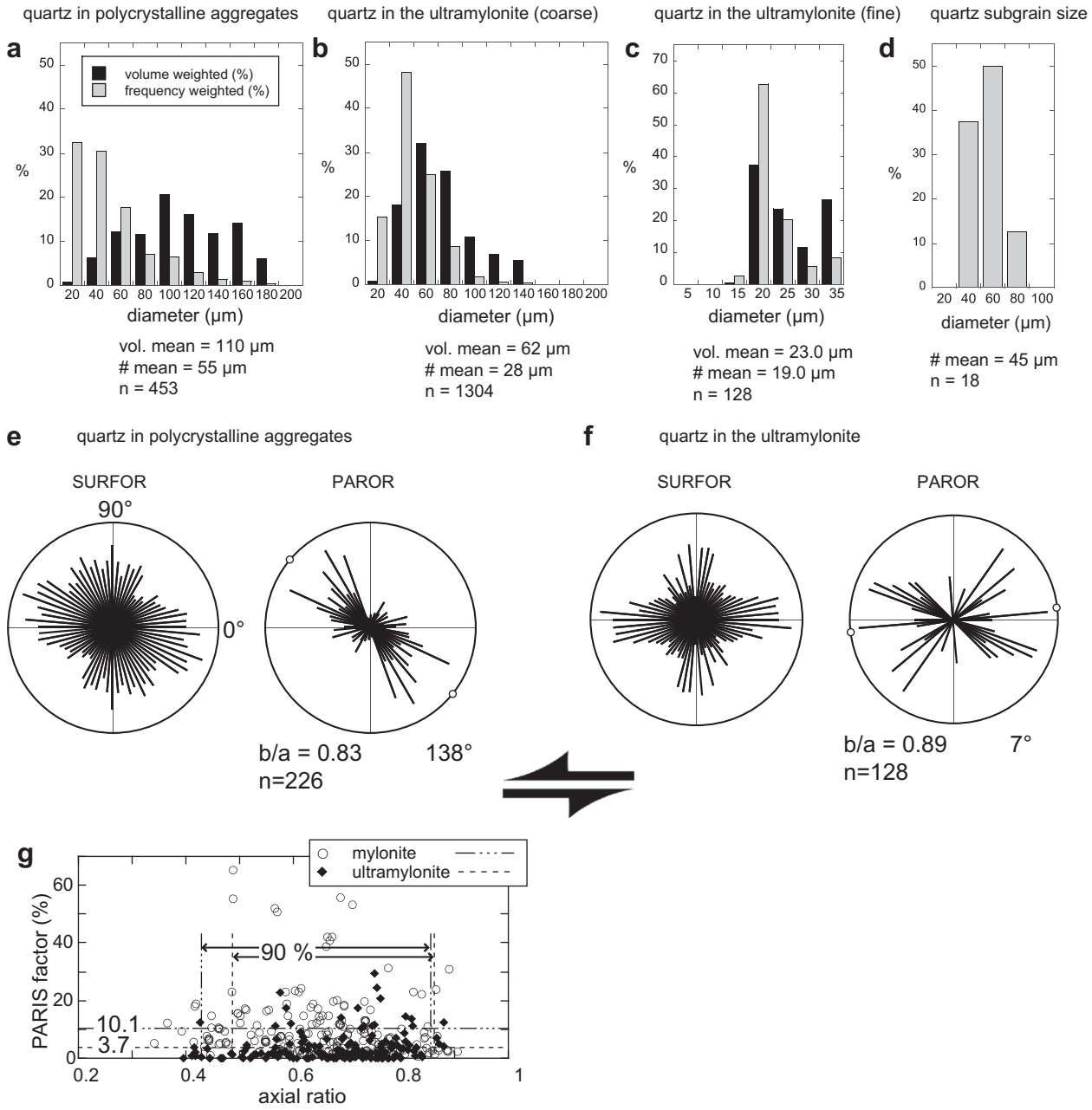

Fig. 6. Quartz grain sizes and fabrics. (a) Quartz grain size distribution of recrystallized grains in the mylonite. Surface (SURFOR) and particle (PAROR) orientation distribution functions. Bulk axial ratio and bulk preferred orientations indicated for the particle fabric. (b) Quartz grain size in the beginning of the ultramylonite after complete phase mixing. (c) Quartz grain size in the finest grained part of the ultramylonite. (d) Subgrain size in recrystallized quartz measured from EBSD maps (boundaries $<7.5°$). Only subgrains bound by at least 2 subgrain boundaries and non-migrated boundaries are considered. Due to the small number ($n = 18$) only the frequency distribution is displayed. (e) Surface (SURFOR) and particle (PAROR) orientation distribution functions of recrystallized quartz in the monomineralic aggregates in the mylonite. (f) Surface (SURFOR) and particle (PAROR) orientation distribution functions of single quartz grains in the ultramylonite. (g) Grain shape diagram of axial ratio versus the PARIS factor (see text). Quartz grains from polymineralic aggregates in the mylonite plot with slightly higher PARIS factors and a larger scatter in axial ratios.

aggregates leads to a complete mixture of the quartz within the matrix phases.

When measured in the mylonite, using a light microscope, the average content of (visible) quartz is 29 ± 2%. Approximately 5% of the quartz is not visible because it occurs as very small grains in the matrix. Correcting for the 'invisible' quartz yields a total quartz content of 30 ± 2%. In the ultramylonite the quartz contents is found to be 31 ± 1.5% (obtained by thresholding of Si-EDS counts).

4.2. Feldspar and mica

The matrix in the mylonite consists of plagioclase (plg), K-feldspar (kfs) and biotite (bt,), with a minor content of white mica (wm) and accessory epidote, clinozoisite, garnet, titanite, and ilmenite; the grain size of most phases is <20 µm. The phases in the mylonite matrix are not homogeneously mixed. Instead, a layering can be observed (Fig. 9a). Fine grained plagioclase (An00 and ~An23) layers are mixed to a variable degree with recrystallized K-feldspar and biotite (Fig. 9a).

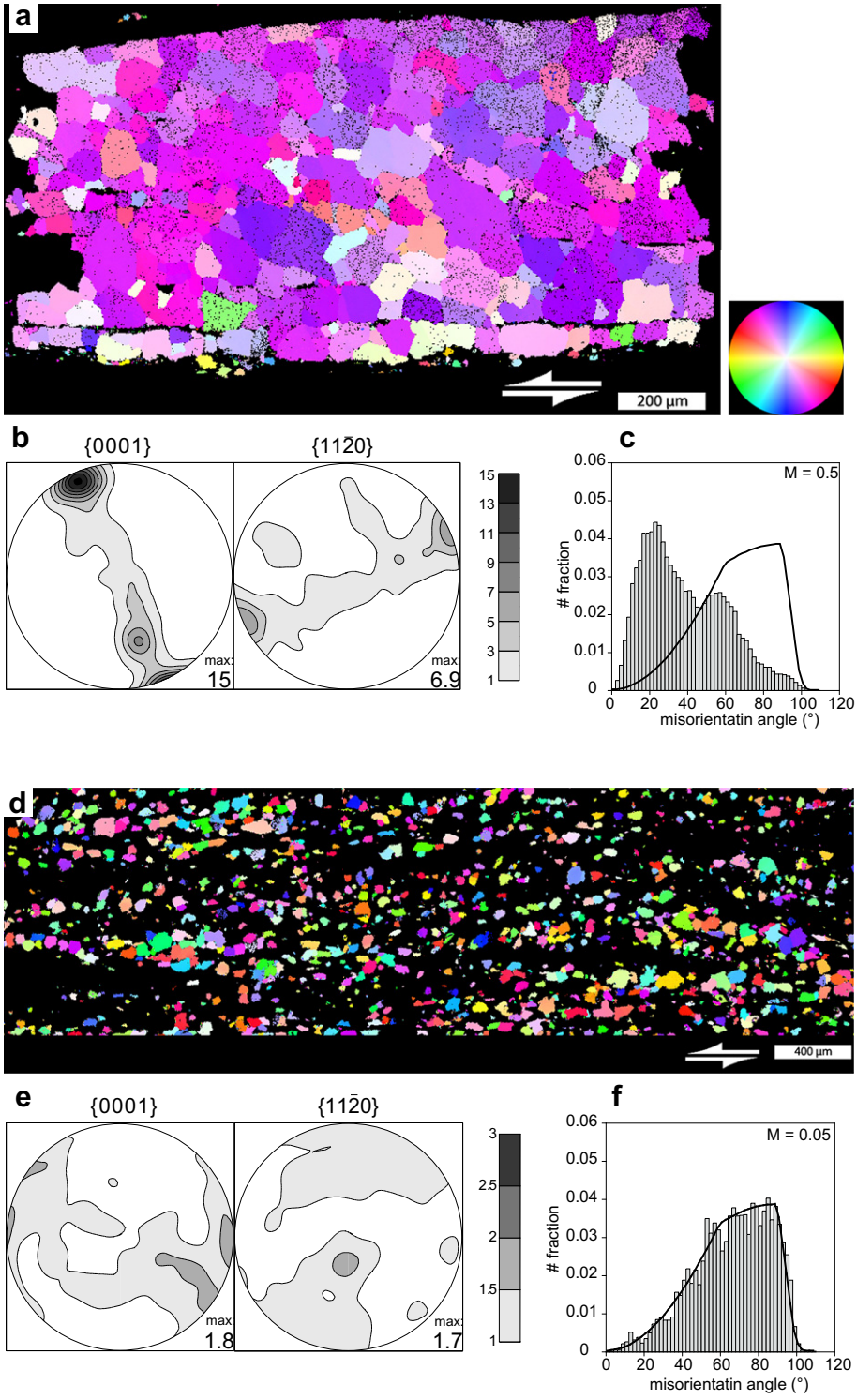

Fig. 7. Quartz crystallographic preferred orientations. (a) C-axis orientation image of dynamically recrystallized quartz in the mylonite. The c-axis orientations recalculated from an EBSD-derived Euler angle image. For grain shape and grain size values see Fig. 6a,e. (b) Pole figures for [c] and <a> axes, calculated from EBSD data at 7.5° kernel halfwidth for quartz in the mylonite. Upper hemisphere, equal area projection. Contours at 2 times uniform distribution. (c) Uncorrelated misorientation of quartz in a polycrystalline aggregate in the mylonite. Solid black line marks the calculated random distribution (see text). M-index = 0.5.(d) C-axis orientation image of Dispersed quartz grains in the ultramylonite. (b) Pole figures for [c] and <a> axes, calculated from EBSD data at 10° kernel halfwidth for quartz in the ultramylonite. Upper hemisphere, equal area projection. Contours at 0.5 times uniform distribution. (c) Uncorrelated misorientation of quartz in the ultramylonite. Solid black line marks the calculated random distribution (see text). M-index = 0.05.

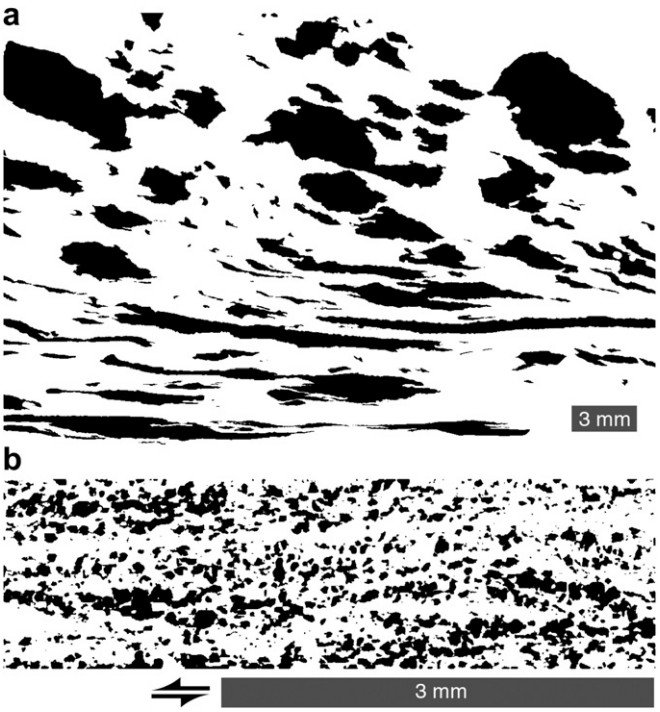

Fig. 8. Quartz maps used to determine quartz volume fractions. (a) Black areas in the upper half are partially recrystallized quartz aggregates and magmatic grains, in the lower half completely recrystallized, polycrystalline aggregates in the mylonite. Quartz content 29 ± 2%. (b) Black areas are quartz, mostly single dispersed grains in the ultramylonite. Quartz content 31 ± 1.5%.

In contrast in the ultramylonite the matrix phases are homogeneously mixed and diluted with the 30% quartz of the mylonite.

Plagioclase in the deformed matrix of the mylonite (see above) appears in the form of oligoclase grains (Ab16–23), with pure albite cores (Fig. 9b). The albite cores are occasionally truncated by grain boundaries parallel to the foliation trace. The core–rim transitions are discrete in plagioclase; gradual changes do not occur (Fig. 9b). The Ca-rich rims display a variable thickness, growing thicker in direction parallel to the foliation.

\Prior to the main deformation, magmatic plagioclase in the protolith is pseudomorphically replaced by fine-grained plagioclase (albite and oligoclase) intergrown with minor amounts of white mica, epidote and clinozoisite. In undeformed plagioclase aggregates ($d \sim 1$–5 mm) white mica is consistently intergrown along the cleavage directions of the former magmatic plagioclase. Observations of the pseudomorphic fine-grained plagioclase aggregates with the lambda plate inserted reveal a crystallographic preferred orientation. With the onset of deformation, all white mica is aligned parallel and the preferred orientation of plagioclase is randomized.

4.2.1. Quantitative microstructures

Albite grains in the plagioclase aggregates of the protolith are almost isometric with an average grain diameter μ_V of 14 μm, an average axial ratio b/a >0.82 and only a weak particle and surface ODF (Fig. 10a).

In the mylonite the plagioclase grains have a μ_V of ~15 μm, and the albite cores of ~10 μm (Fig. 10b,c). Comparing the PAROR and SURFOR results of the whole grains with those of the albite cores, one finds that the bulk axial ratio of the grains is lower (b/a bulk = 0.49) indicating a more elongated shape while that of the albite cores is higher (b/a bulk = 0.59) (Fig. 10b,c). The ODFs of the long axes of the grains and the cores show an orientation of 171° and 4° respectively.

Plagioclase grains in the ultramylonite have a μ_V, of 15.0 μm (Fig. 10d). The plagioclase shows a strong grain shape preferred orientation with an orthorhombic particle ODF and a bulk axial ratio of ~0.54. Particle long axes are inclined very slightly (176°) with respect to the foliation (Fig. 10c,d).

K-feldpar in the mylonite resembles very much plagioclase (Fig. 9b). Tails of recrystallized K-feldspar ($d \sim 10$–20 μm), are mixed into the matrix. K-feldspar clasts of the protolith are occasionally replaced by myrmekite which is an additional source for fine grained plagioclase and quartz (Menegon et al., 2006). The mean diameter, μ_V, of K-feldspar is ~15 μm and constant throughout the entire ultramylonite (Fig. 10e). Grains show a preferred particle elongation subparallel to the foliation and yield a bulk axial ratio of ~0.52. Particle long axis is aligned at a small angle (~175°) with respect to the foliation. The surface ODF has an orthorhombic or monoclinic symmetry and shows a secondary maximum normal to the foliation (Fig. 10e).

K-feldspar grains occur in layers of quartz, plagioclase, plagioclase and biotite, or in entirely mixed layers. Isolated K-feldspar often fills the space between quartz grains (Fig. 11). All of the fine-grained K-feldspar in the ultramylonite is derived from

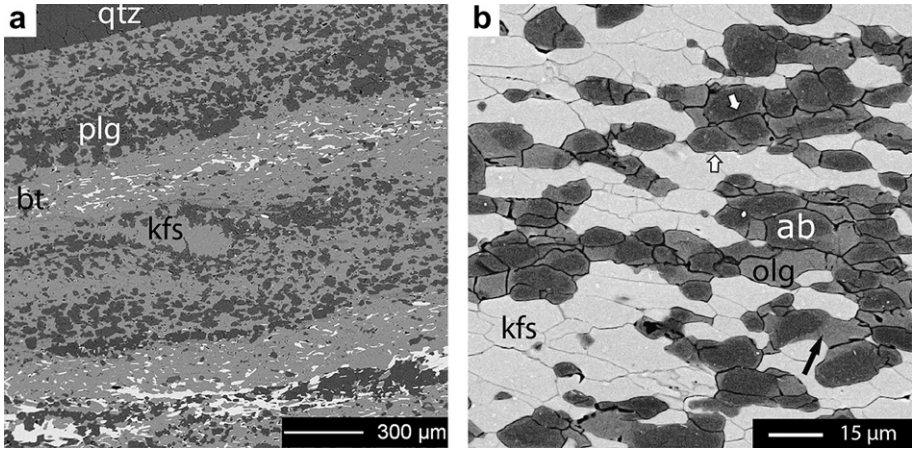

Fig. 9. Matrix in the mylonite: (a) Polymineralic matrix showing a compositional layering, consisting of plagioclase (dark grey), K-feldspar (medium-grey) and biotite (white). The dark grey layer at the top is a polycrystalline quartz aggregate. (b) K-feldspar - plagioclase aggregate of the matrix. Cores of plagioclase consist of albite, rims of oligoclase. Note preferential growth of rims parallel to the grain shape defined foliation (black arrow) and the truncation of cores against phase and grain boundaries normal to the foliation (white arrows). SEM/BSE) images. qtz: quartz, kfs: K-feldspar, bt: biotite, plg: plagioclase, ab: albite, olg: oligoclase.

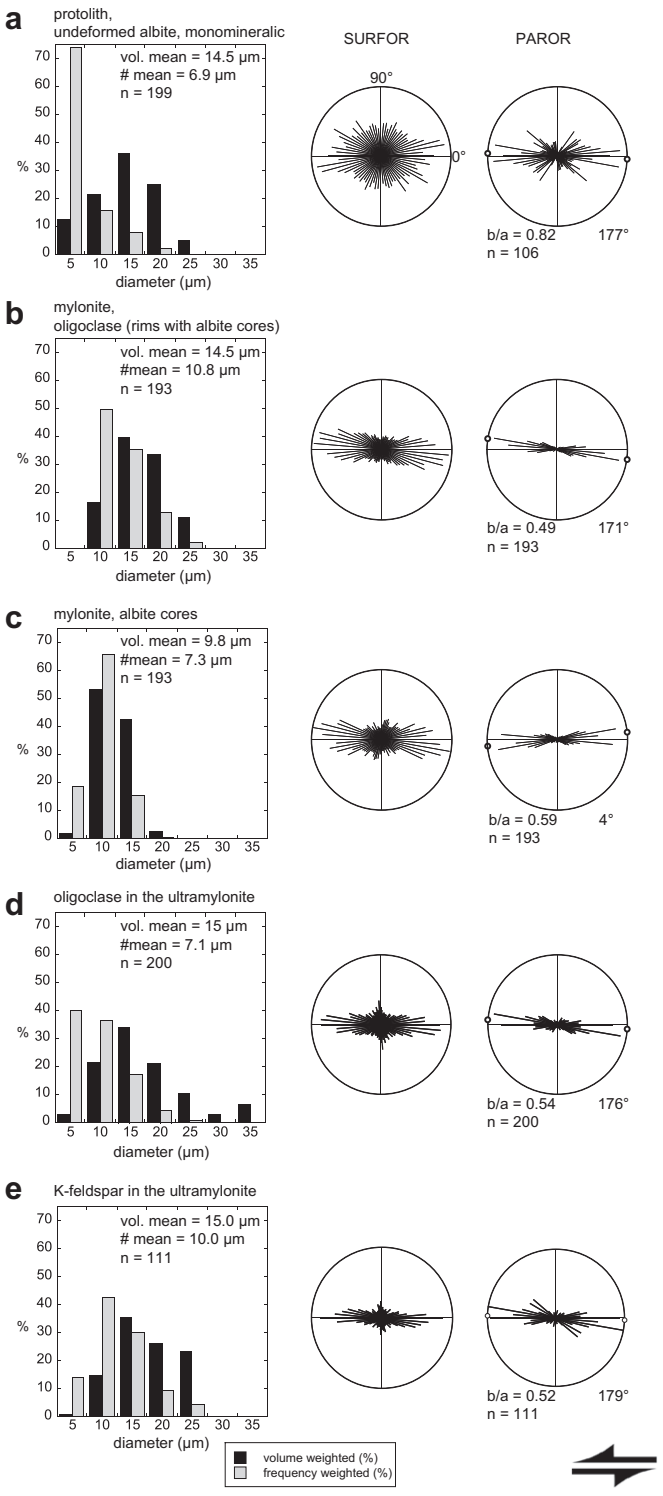

Fig. 10. Feldspar grain size distributions and surface (SURFOR) and particle (PAROR) orientation distribution functions. Bulk axial ratio and bulk preferred orientations indicated for the particle fabric. (a) Albite grains from a monomineralic aggregate in the protolith (assumed to be undeformed by the shear zone). (b) Deformed plagioclase grains of the matrix of the mylonite with synkinematically grown oligoclase rims. (c) Albitic cores of grains from b). (d) Oligoclase from the ultramylonite. (e) K-feldspar from the ultramylonite preferentially adjacent to quartz grains. For the corresponding microstructures of b,c) see Fig. 9b and for d,e) see Fig. 5b.

recrystallization or solution – precipitation (Figs. 5 and 11c,d) though a very minor amount of relict grains may be present. Non-recrystallized K-feldspar clasts are only rarely preserved in the ultramylonite; some show myrmekite formation in the close vicinity of K-feldspar precipitation sites (Fig. 11e). The shape of the phase boundaries between quartz and K-feldspar indicates the precipitation of K-feldspar in strain shadows and dilatant sites within these layers (Fig. 11a–d).

The average PARIS factors of plagioclase (~8%), K-feldspar (~10%) in the ultramylonite is larger compared to quartz (~4%), as well as the smaller bulk axial ratio of the feldspar grains indicate quartz is almost equiaxed and fully convex while the feldspar grains are more elongated and slightly lobate (compare Fig. 5b).

Most mica in the mylonite is a brown biotite which is originally recrystallized from magmatic biotite in the protolith (Menegon et al., 2006) though white mica is also occasionally present in the matrix. Recrystallized biotite forms layers in the mylonite or occur as isolated flakes (Fig. 9). Biotite layers disappear with increasing strain. In the ultramylonite single grains are isolated between quartz, plagioclase and K-feldspar (Fig. 5). Kinking and folding of the dispersed grains is not observed. Together with K-feldspar, some biotite flakes occur as bridges between quartz grains (Fig. 5b). Biotite grains have an average length in the same size range as that of the other matrix phases (10–30 µm).

4.3. Transition zone

The transition zone from the mylonite to the ultramylonite (Fig. 2) is defined as the zone where quartz aggregates disintegrate. Throughout the transition zone changes in texture, microstructure, grain size and spatial distribution of the different phases can be observed.

The transition from polycrystalline aggregates to single dispersed grains is accompanied by a switch from a monoclinic to an orthorhombic geometry of the quartz surface ODF together with a decrease of the bulk axial ratios (Fig. 6e,f). While the quartz grain size is constant in the mylonite (110 µm), it decreases to about 20 µm in the ultramylonite and approaches the matrix grain size (e.g. plagioclase μ_V = 15 µm, Fig. 5, 6). The grain size decrease begins with the disintegration of the quartz aggregate and continues into the ultramylonite.

At the beginning of the transition, near the mylonite quartz aggregates are highly deformed and occur as increasingly thinned layers. At first, isolated K-feldspar can be found in triple junctions, triple (and quadruple) junctions of smaller grains, grain boundary jogs and along aligned grain boundaries of large grains (Fig. 12a). Increasing amounts of K-feldspar coincide with straight aligned grain boundaries, which may be continuous over several grains. K-feldspar also forms thin foliation-parallel, discontinuous seams inside elongate quartz aggregates (Fig. 12a) often grading into continuous K-feldspar seams. From these seams small fin-shaped K-feldspar protrudes between quartz grains, along (sub)grain boundaries, and, in rare cases, also directly into quartz grains (Fig. 12b). The protrusions are often asymmetric; the asymmetry shows a synthetic orientation with the sense of shear. Similar structures also form at the edges of the quartz aggregates (Fig. 12c). K-feldspar seams inside quartz aggregates may originate from the tails of K-feldspar fish embedded in a quartz layer, but the seams generally occur relatively isolated. The local crystallographic orientation of the smaller quartz grains adjacent the K-feldspar seams is often rotated with respect to the overall CPO and the quartz grain size is locally decreased in such cases (Fig. 12a).

The quartz CPO in the transition zone shows a considerably weaker and inclined peripheral *c*-axis maximum compared to that of the mylonite, and the angle between the foliation and the *c*-axis

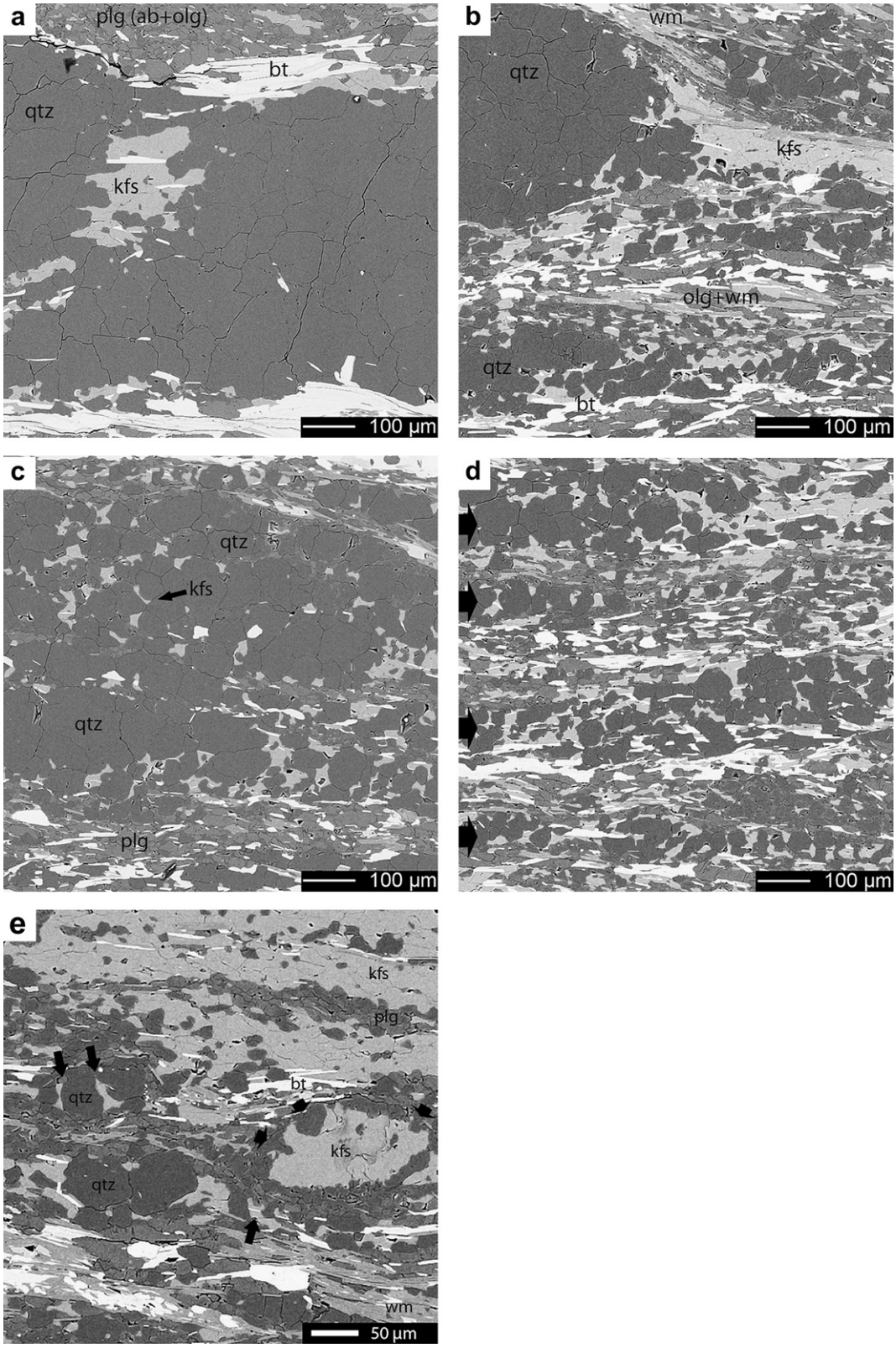

Fig. 11. Evolution of microstructures in the transition from mylonite to ultramylonite. (a) Mylonite. Rare localized boudinage of polycrystalline quartz layer with K-feldspar precipitation in the neck. (b) Grain separation at the edge of a relict quartz aggregate by K-feldspar precipitating along grain boundaries. (c) Homogeneous K-feldspar precipitation at triple junctions and grain boundaries inside a quartz aggregate. (d) Layers of dissected quartz aggregates (indicated by arrows) and K-feldspar precipitates. (e) Relict K-feldspar clast, replaced by myrmekite (short arrows) and adjacent K-feldspar precipitation between quartz grains (long arrows). Near top of image a recrystallized K-feldspar layer with plagioclase grains. All SEM/BSE images. Sinistral shear sense. For location see Fig. 2. qtz: quartz, kfs: K-feldspar, plg: plagioclase, ab: albite, olg: oligoclase, bt: biotite, wm: white mica.

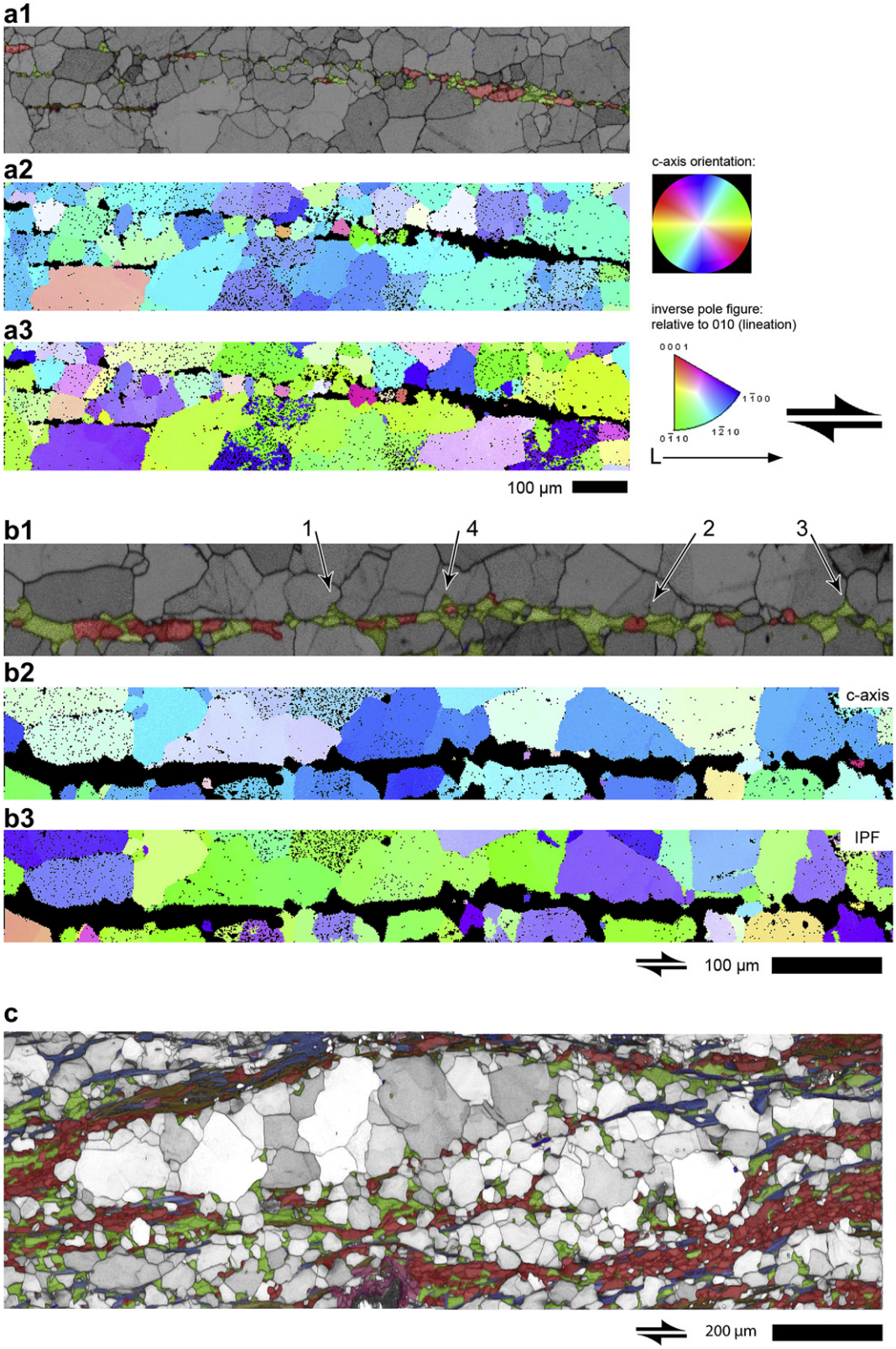

Fig. 12. (a,b) Quartz layers with layer parallel, heterogeneous K-feldspar, biotite and plagioclase seams, found in the highest strained mylonite/beginning of the transition zone. (a1,b1) EBSD image quality map overlain by EDX-derived combined element map. Red: Al–Na counts (albite, oligoclase), green: K counts (K-feldspar), blue: Fe + Mg counts (biotite), brown: mica, grey: quartz. Straight line cutting across grain boundaries are surface scratches of the sample. (a2,b2) Quartz *c*-axis orientation map. (a3,c3) Quartz inverse pole figure map. Reference direction is the lineation L. Precipitation occurs at triple junctions and aligned grain boundaries. The quartz grain size is locally decreased due to pinned grain junctions and boundaries. Note small quartz grains surrounded by the K-feldspar precipitates are rotated with respect to their neighboring grains. (b) K-feldspar and plagioclase layer within quartz aggregate developing fin-shaped protrusions between quartz grain boundaries (1), subgrain boundaries (2), dauphine twin boundaries (3) and occasionally into grains (4). Some fins show an asymmetry consistently related to the sense of shear. Maps and color look-up tables are the same as in figure (a). (c) Disintegrating quartz aggregate in the transition from mylonite to ultramylonite. EBSD image quality map overlain by EDX-derived combined element map. Red: Al–Na counts (albite, oligoclase), green: K counts (K-feldspar), blue: Fe + Mg counts (biotite), brown: white mica, grey: quartz. K-feldspar and biotite occupy predominantly the space between quartz grains (grey-white).

maximum decreases to a value of 120°–140° (Fig. 13). The difference corresponds to a synthetical rotation of the *c*-axis pole figure with respect to the sense of shear.

By calculating grain-size-dependent CPOs it can be seen that the preferred orientation is restricted to the fraction of larger quartz grains (e.g. $d > 60$ μm) (Fig. 13b) both in number-weighted and in area-weighted pole figures. The grain size of 60 μm was chosen as it is the largest grain size fraction in the ultramylonite. Furthermore, it is the size of grains of the most elongate quartz aggregates, i.e., of the layers which are only one or two grains thick. Grains with $d < 60$ μm reproducibly show a nearly random distribution. Randomness was tested by comparing the measured maxima with the corresponding values of a random orientation distribution function of the same size (number of grains) using the same kernel width.

The incipient K-feldspar precipitation between quartz grains produces a different microstructure than dynamic recrystallization. Initial K-feldspar precipitates show a particle ODF with a maximum at an angle to the foliation (22°), inclined against the sense of shear (Fig. 14a,b). With increasing grain separation or by relative rotation of the phase boundaries during progressive shear the K-feldspar long axes become oriented subparallel to the foliation.

Phase boundaries between quartz, K-feldspar and plagioclase are often lobate. Small plagioclase grains often bulge into quartz grains (Fig. 14c). Quartz-K-feldspar boundaries are often smoothly curved with the K-feldspar forming convex protrusions into the quartz grains (Fig. 14d–f). The opposite case is much less frequently.

4.4. Quartz distribution

The spatial distribution of phases can be seen on phase maps. These were prepared for quartz, plagioclase, K-feldspar, biotite and white mica (Figs. 15a and 12c). The micas are grouped together as they are rather homogeneously distributed among the other phases and no major differences in microstructural properties are observed. In the transition between mylonite and ultramylonite, quartz-rich areas are predominantly associated with K-feldspar and quartz–plagioclase-mixtures are rare, so that quartz, plagioclase and K-

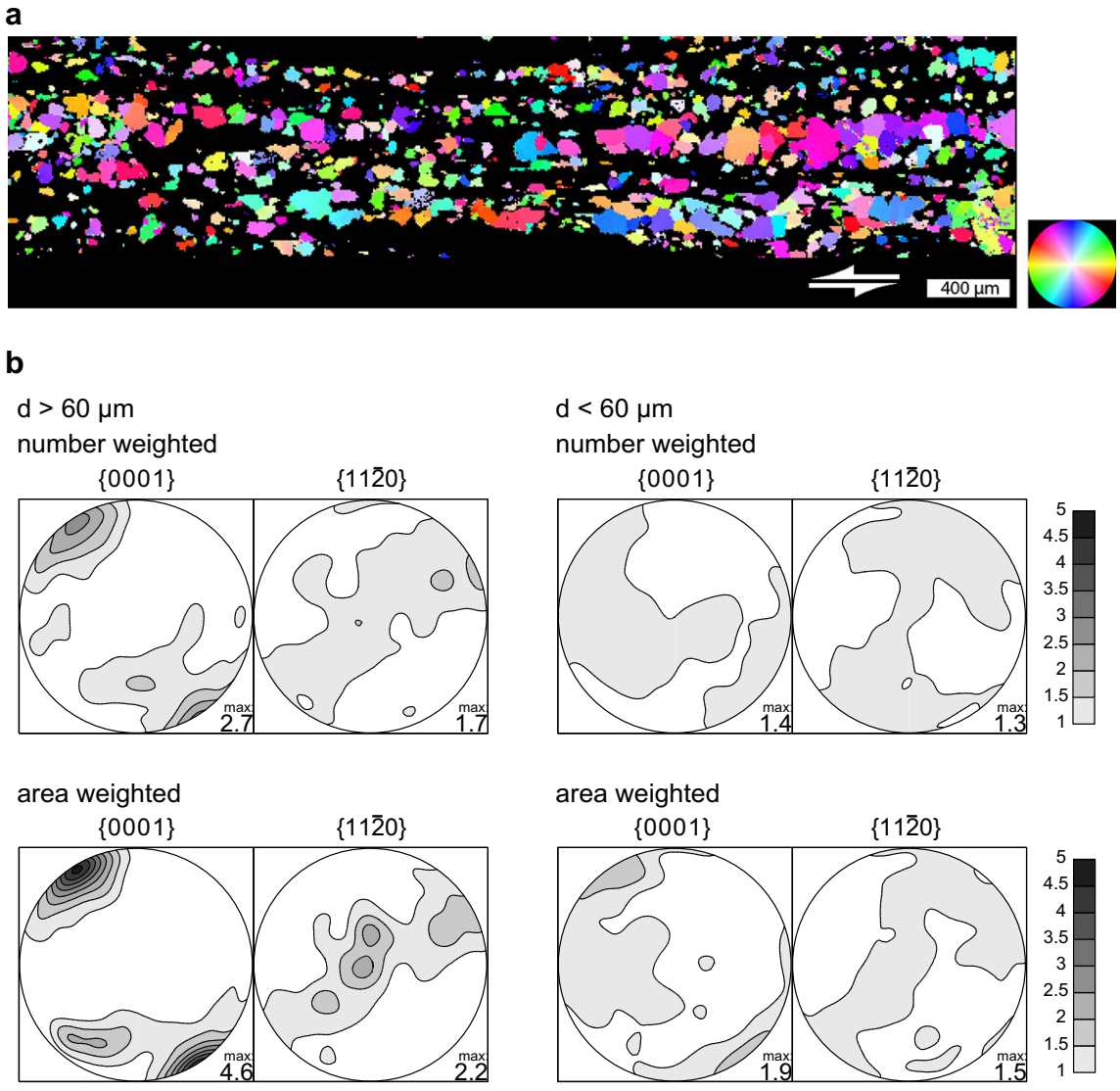

Fig. 13. Disintegrating quartz aggregates. (a) C-axis orientation image showing a relict quartz layer in the transition from the mylonite to the ultramylonite. (b) Number and area-weighted pole figures for [c] and <a> axis orientation for grains larger ($n = 1224$) and smaller ($n = 7002$) than 60 μm, 10° kernel halfwidth. Contours from 1 at 0.5 times uniform distribution. The weak c-axis maximum originates from relict layers, exemplarily shown in 13a (purple, see color LUT). The increase of the maxima from number to an area-weighted pole figure indicates that the small grains are more randomly oriented than the larger ones.

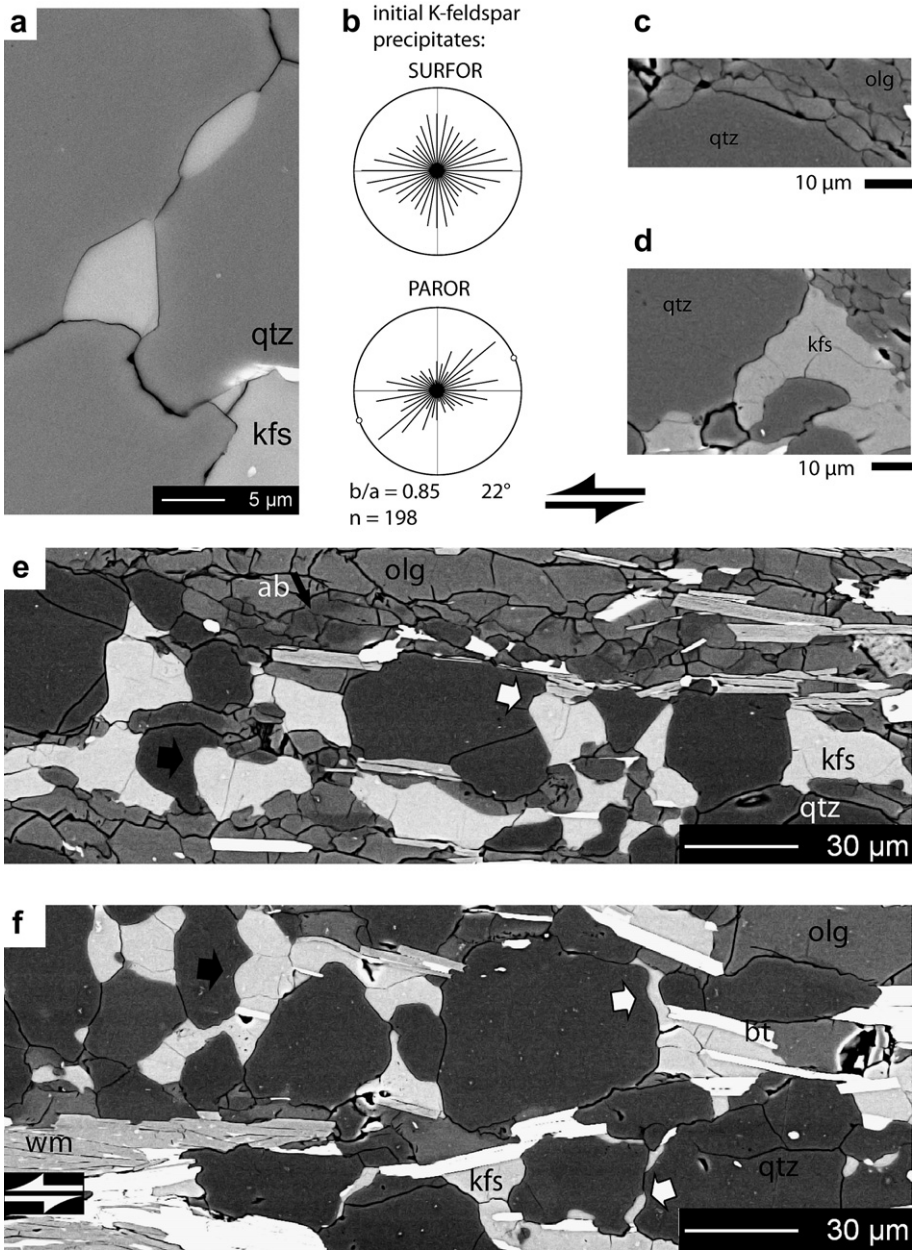

Fig. 14. K-feldspar precipitation and phase boundary migration. (a) Initial K-feldspar precipitation between quartz grains in a polycrystalline quartz aggregate in the mylonite. (b) Surface (SURFOR) and particle (PAROR) orientation distribution function of K-feldspar precipitates during initial quartz aggregate disintegration, comparable to a) (e.g. Fig. 11c). (c) Oligoclase matrix grains bulging into a quartz grain in the mylonite. (d) K-feldspar grows in the quartz aggregate along former quartz grain boundaries. The phase boundary shows an undulatory, lobate structure while quartz grain boundaries commonly are smooth. (e,f) Quartz layers being disintegrated by K-feldspar precipitation. e) layer less stretched; f) layer more stretched. In some cases the shape of former quartz grain boundaries is still recognizable (white arrows); K-feldspar bulging into quartz grains (black arrows). All SEM/BSE images. qtz: quartz, kfs: K-feldspar, ab: albite, olg: oligoclase, bt: biotite, wm: white mica.

feldspar do not occur in a random distribution of all three phases. In the layers with the smallest grain size and the highest degree of mixing, quartz grains often align with K-feldspar parallel to the foliation in a festoon-like geometry (Figs. 11d and 15a). As a geometrical consequence of the thinning of the quartz-K-feldspar layer, the foliation-parallel contact-area with plagioclase is increased.

Here, we use a modified phase distribution analysis that is based on Rgp versus grain size plots of quartz (Fig. 15b). In a number of microstructurally homogeneous areas with a narrow grain size distribution, Rgp for disintegrating quartz aggregates were determined. Rgp and the mean quartz grain sizes were measured and plotted (Fig. 15b). With decreasing mean grain size, the ratio Rgp of grain to phase boundary area decreases indicating a higher degree of mixing. The minimum grain size possible to analyze depends on the step size of the EBSD maps (1,2,4.5 µm). Linear fits are only calculated for areas obtained within the same map. A correction for different step sizes has been applied for Fig. 15c (see below) and the minimal grain size was 12 micron.

5. Discussion

The following discussion is in part based on an interpretation of the strain gradient in the analyzed shear zone. Generally, a strain gradient in shear zones can result from (1) a gradient in

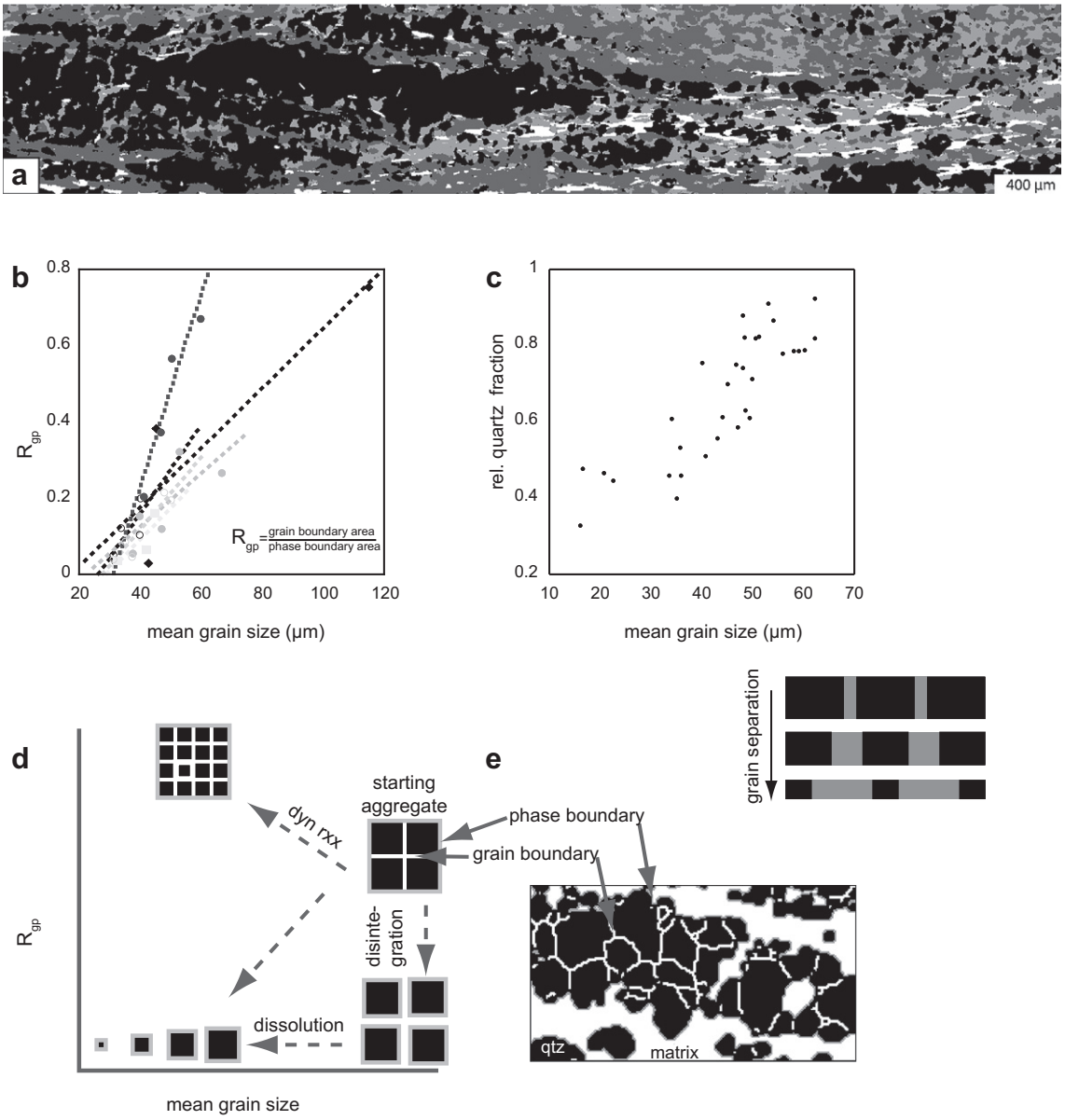

Fig. 15. Phase distribution and grain size evolution. (a) Phase map of quartz (black), plagioclase (dark gray), K-feldspar (light grey) and mica (white). The map shows a quartz aggregate in the transition between the mylonite and the ultramylonite with different stages of disintegration. (b) Rpg (ratio of grain boundary/phase boundary area) versus the mean grain size in 6 different, laterally disintegrating aggregates. Symbols correspond to individual, homogenous aggregates. (c) Relationship between the mean quartz grain size in a layer and the relative quartz volume fraction. The relative quartz volume fraction in a layer decreases with increasing disintegration, as grains are separated by K-feldspar. In layers with a higher grain separation the mean grain size is smaller. (d) Schematic model of Rpg – grain size evolution. Black squares are separated from another by grain boundaries (white) and from the matrix by phase boundaries (dark grey) (e) Example of an analyzed area. The evaluation of Rpg and the grain size would correspond to a single point in the diagram b).

the shear strain rate while the whole shear zone is deforming, or (2) from localization of deformation in the internal parts of the shear zone at later stages of the deformation (type II, Hull, 1988; Means, 1995), or (3) the shear zone widens with time due to strain hardening so that the outer parts represent later strain increments (type I of Hull, 1988; Means, 1995). The third possibility can be excluded here because of the lack of flat-topped strain profiles and the fact that strain hardening is very unlikely in the center of the shear zone (see below). The two first possibilities are end member cases and natural shear zones may result from a combination of both. A faster shear strain rate can be caused by a change of rate controlling parameters (e.g. CPO, permeability, bulk diffusivity) or by a switch in the dominant deformation mechanism. As most of these parameters in the Gran Paradiso shear zones are strain-dependent or a consequence of microstructural development (e.g. CPO, SPO, reaction products), we assume that the structures developed along the strain gradient primarily record a progressive strain history (type II shear zones). This implies that microstructures preserved near shear zone center represent later stages, whereas the microstructures near the shear zone margins represent earlier stages of the deformation history obliterated during subsequent strain localization in the shear zone center.

In the following we will discuss the process of progressive phase mixing, the deformation mechanism in the mylonite and ultramylonite, and the processes involved in the grain size reduction. Finally we will evaluate possible reasons that may cause the phase mixing and rheological implications.

5.1. Phase mixing

The transition from the mylonite to the ultramylonite takes place across a continuous transition zone. Polycrystalline quartz aggregates preferentially disintegrate at grain boundaries which are (sub)perpendicular to the layering by K-feldspar or biotite precipitating in dilatant sites (Figs. 11, 14a,e,f, and 15a). One grain thick quartz layers only occasionally persist up to very high strains. Oligoclase is rarely found between dilatant quartz grain boundaries. The effect of quartz layer disintegration is particularly prominent in high-strain layers, which are only one single grain wide (Fig. 14e,f). Inside the quartz aggregates, K-feldspar is found either in triple (quadruple) junctions, grain boundary jogs and along grain boundaries oriented at a large angle to the inferred stretching direction (e.g. Figs. 11, 12a,b and 15a,e). The latter sites occur preferentially along the aggregate periphery and discrete seams (at lower strains; Fig. 12a,b), or are homogeneously distributed across the entire aggregate (Fig. 11c). The location, shape, and distribution indicate that the K-feldspar and biotite grains must have nucleated in place (gbs; Figs. 5b, 11a,c and 14e,f). The distribution and shapes of K-feldspar occurrences resemble very much those of the voids observed by Ree (1994) in grain boundary sliding experiments of octachloropropane (e.g. Fig. 7/8 of Ree, 1994) produced during neighbor switching events.

Cavitation is used to describe the process of the formation of dilatant sites (e.g. Pilling and Ridley, 1988; Ayensu and Langdon, 1996). These sites can be caused by heterogeneous deformation at the grain scale, for example during grain boundary sliding (e.g. Pilling and Ridley, 1988; Ree, 1994; Ayensu and Langdon, 1996; Zhang et al., 1996). Empty pores (cavities) have been observed in rock deformation experiments (Rybacki et al., 2008) and may occur in naturally deformed rocks (Fusseis et al., 2009). However, if the rate of precipitation of intergranular material can occur at a rate that is at least equal to the opening rate, empty voids will not form. Nevertheless, the process of the formation of dilatant sites is very similar to cavitation.

The location of K-feldspar nucleation apart from an adjacent source of potassium and aluminum requires that material transport must have taken place by grain boundary diffusion or, more likely, in a grain boundary fluid film. Only in a few cases, layer parallel seams inside quartz aggregates are formed as tails of small K-feldspar sigma-clasts. Therefore, we infer that the major part of intergranular material inside the quartz aggregates must have formed by syndeformational nucleation and growth. Similar inferences have been made for for K-feldspar in granitoid mylonites (Behrmann and Mainprice, 1987; Ishii et al., 2007), amphibole growth in mafic mylonites (Boullier and Gueguen, 1975; Kruse and Stünitz, 1999) and mica in calcite mylonites (Herwegh and Jenni, 2001). With increasing strain the amount of K-feldspar and biotite situated between quartz grains increases as documented by increasing distances between grains and an increasing fraction of separated quartz grain boundaries (Fig. 15a,b). In addition, the lobate morphology of some quartz-K-feldspar boundaries indicates that phase boundary migration has taken place (Fig. 14) as previously observed in mylonites by Gower and Simpson (1992) and Stünitz and Fitz Gerald (1993). This aspect will be considered below in more detail.

5.2. Deformation mechanisms

Most of the quartz in the mylonite occurs in polycrystalline aggregates which have formed by dynamic recrystallization of the magmatic quartz. The fine-grained matrix in the mylonite originates from different processes: dynamic recrystallization (bt, kfs), myrmekitic feldspar reaction (plg, qtz, wm) during deformation (Menegon et al., 2006, 2008), precipitation (kfs, bt) and earlier static (non-deformational) recrystallization (plg, wm) of the protolith.

5.2.1. Quartz in the mylonite

In the mylonite, polycrystalline, monophase quartz aggregates deform by dislocation creep as indicated by a strong CPO (Fig. 7a,b,c), an asymmetric, monoclinic surface ODF (Fig. 6e), and microstructures typical for subgrain rotation recrystallization with extensive grain boundary migration. The CPO type is attributed to a dominant activity of the basal <a> glide system (Schmid and Casey 1986). Prism-parallel subgrain boundaries are consistent with the activity of the basal <a> slip system in the case of tilt walls made up of edge dislocations (Trepied et al., 1980). However, the activity of the basal <a> glide system is usually described from instances of deformation temperatures lower than in the Gran Paradiso rocks (e.g. Stipp et al., 2002).

The dynamically recrystallized grain size of monomineralic quartz aggregates is stable across the entire strain gradient of the mylonite. The quartz subgrain size is smaller than the recrystallized grains size (Fig. 6a,d). Grain boundary morphology and grain shapes indicate that excessive grain boundary migration (e.g. Guillope and Poirier, 1979; Poirier and Guillope, 1979; Jessell, 1987) occurred in addition to subgrain rotation. In early stages, K-feldspar (±biotite) precipitates occur as isolated grains along quartz grain boundaries (Fig. 12a,b). With increasing strain these K-feldspar precipitates connect along grain boundaries (Figs. 11 and 12). An alignment of grain boundaries parallel to the displacement direction (Figs. 4a,b and 12a,b) is frequently reported in materials deforming with a contribution of grain boundary sliding (e.g. Drury and Humphreys, 1988; Stünitz and Fitz Gerald, 1993; Fliervoet et al., 1997). The occurrence of quadruple junctions (Fig. 13a) can also be taken as an indication of grain boundary sliding (e.g. Ashby and Verrall, 1973; Goldsby and Kohlstedt, 2001) as well as the occurrence of mineral precipitates along certain grain boundary orientations (e.g. Fig. 14a,b) in quartz (e.g. Behrmann and Mainprice, 1987). Thus, the quartz-k-feldspar-biotite-microstructures indicate that some grain boundary sliding has taken place during dislocation creep deformation of the quartz aggregates.

5.2.2. Matrix phases

The fine grained albitic plagioclase in the protolith and the mylonite matrix is assumed to be a product of the static HP metamorphism and is not related to dynamic recrystallization, because fine grained albite is also present in the undeformed parts of the protolith. The static decomposition of plagioclase into fine-grained aggregates which pseudomorphically replace igneous grains has been observed elsewhere in situations where high pressure metamorphism is preserved in low strain domains (e.g. Lenze and Stoeckhert, 2007).

Plagioclase in the matrix remains at a constant size in the mylonite, in the transition zone, and in the ultramylonite (Fig. 10a,b,d). With the onset of deformation in the mylonite albite is synkinematically replaced by oligoclase, and the plagioclase grains change their shape toward more elongated grains. Albite cores are truncated at their long sides by grain boundaries and oligoclase replacement and/or overgrowth occurs at the ends of grains parallel to the stretching direction. The nearly constant grain size of undeformed plagioclase and the plagioclase in the mylonite suggests a process of replacement or dissolution and precipitation for the core − rim formation rather than grain growth during the change of shape (Figs. 9b and 10a,b,c). These microstructures indicate diffusion creep deformation. The change in the plagioclase composition is related to a decrease in pressure or an increase in temperature (LeGoff and Ballevre, 1990; Brouwer et al., 2002) before or during the onset of the shear zone formation.

Fine-grained biotite in the mylonite results from dynamic recrystallization of primary magmatic biotite (e.g. Menegon et al., 2006). Biotite (and minor white mica) recrystallized grain size remains constant in the mylonite and ultramylonite. Kinking of grains and the formation of interconnected layers (features common in crystal plastic deformation of mica; (Kronenberg et al., 1990; Holyoke and Tullis, 2006)) are not observed in the ultramylonite. Instead, with increasing strain, a portion of biotite is found between quartz grains where it must have formed by precipitation. Similar distributions of micas have been reported for rocks undergoing diffusion creep (e.g. Fliervoet et al., 1997; Herwegh and Jenni, 2001). Thus, the observed mica fabrics suggest diffusion creep rather than dislocation creep deformation.

K-feldspar matrix grains initially form recrystallized layers, occasionally intermixed with minor albite/oligoclase. The plagioclase in these layers is in part of myrmekitic origin (Menegon et al., 2006), in part perthitic. Diffusion creep has been identified as the dominant deformation mechanism in the monomineralic fine grained K-feldspar aggregates (Menegon et al., 2008). The K-feldspar grain size and grain shapes are comparable to that of plagioclase (Fig. 9b). In summary, it is concluded that the microstructures of each of the phases K-feldspar, plagioclase and biotite and all phases as a mixture indicate diffusion creep deformation.

5.2.3. Deformation mechanism in the ultramylonite

The transition from a mylonite to ultramylonite marks the transition from a 2-phase rheology to a single-phase rheology material (ultramylonite). The quartz aggregates are disintegrated (Figs. 11 and 15), the quartz grain size has decreased toward the matrix grain size (Fig. 6a,b,c), the quartz grain shapes have changed from a monoclinic to a more isometric, orthorhombic geometry, (Fig. 6e,f) and the CPO is almost destroyed (Fig. 7b). The very weak residual CPO shows a small angle between the very weak *c*-axis maximum and the elongation direction. Such quartz fabrics have been observed in low-grade rocks deformed by diffusion creep (Hippertt, 1994; Stallard and Shelley, 1995). A crystallographic control of dissolution–precipitation processes has also been proposed to be capable of producing a CPO (Bons and den Brok, 2000). Note, however, that the strength of the CPO is too weak to be interpreted with any level of confidence. Apart from the dispersion of about 30 volume percent quartz into the matrix and complete mixing of phases, the microstructural characteristics of the former matrix minerals do not change in the ultramylonite. From all the fabric characteristics it is concluded that the entire ultramylonite deforms by diffusion creep.

Despite the decreased quartz grain size, dispersed quartz grains still show a surface and particle ODF different from the other matrix minerals (Figs. 6f and 10d,e). The more equant shape of quartz grains can either be interpreted as a relict or alternatively result from grain rotation during diffusion creep of the matrix. Quartz grains in the ultramylonite are traced by tails of K-feldspar and biotite precipitates (Fig. 5b). This may be taken as an indication that quartz still constitutes a mechanically stronger phase inside the ultramylonite.

5.2.4. Feldspar grain shape anisotropy and diffusion creep

Rocks deforming by diffusion creep with a dominant contribution of grain boundary sliding often show equant grain shapes (e.g. Boullier and Gueguen, 1975; Fliervoet et al., 1997; Kruse and Stünitz, 1999). A weak CPO and SPO in high temperature deformation may be attributed to diffusion creep including relative grain rotation during grain boundary sliding. In plagioclase experimentally deformed by diffusion creep, a well-defined grain shape anisotropy and SPO have been observed (Barreiro et al., 2007). The authors consider grain boundary sliding and alignment of minerals with a shape anisotropy to produce the SPO. In the Gran Paradiso mylonites the plagioclase grain shapes are dynamically modified during deformation and show a strong grain shape anisotropy and an anisotropic particle and surface ODF (Figs. 9b and 10). As long as rotation rates are low enough, dissolution–precipitation may lead to anisotropic grain shapes in non-coaxial flow (e.g. Bestmann et al., 2004). Theoretical considerations (Wheeler, 1992, 2009) suggest the formation of an SPO during diffusion creep at low rotation rates and if grain growth rates are low compared to the rate of diffusion. We observe a constant plagioclase grain size and plagioclase shape changes that involve diffusive mass transfer. Thus, the development of a strong SPO in matrix minerals and deformation by diffusion creep and grain boundary sliding are consistent in the case of the Gran Paradiso rocks at low grain rotation rates.

5.3. Grain size reduction

5.3.1. Grain size reduction and phase separation

The grain to phase boundary area ratio Rgp and the quartz fraction of a layer both decrease with decreasing grain size (Fig. 15b,c), indicating that grain size reduction of quartz and mixing of phases occur simultaneously. There are two processes which can be considered for grain size reduction or the disintegration of quartz layers, as shown schematically in Fig. 15d: (1) Subgrain rotation recrystallization may reduce the grain size but do not cause a phase separation and Rgp should increase. (2) If only phase separation (e.g. nucleation of second phases at triple junctions and grain boundaries) occurs, it will require an additional process such as, e.g. dissolution to reduce the grain size subsequently. Fracturing is also a process that would result in a grain size decrease but with respect to the low differential stresses and the lack of microstructural evidence it is considered as very unlikely.

The dominant grain size-controlling process in quartz is dynamic recrystallization producing a constant grain size in the monomineralic quartz aggregates. Both, subgrain rotation and grain boundary migration recrystallization are inferred to operate together as recrystallization mechanisms. Grain boundary migration is generally inferred to follow the nucleation of new grains by subgrain rotation (e.g. Poirier and Guillope, 1979), leading to grain coarsening (e.g. Mercier, 1980; Poirier, 1985; Urai et al., 1986; Knipe and Law, 1987; Bons and Urai, 1992). The constant grain size along the strain gradient in the mylonite indicates that the recrystallization mechanisms are in a dynamic equilibrium with the flow stress (e.g. Goetze and Kohlstedt, 1973; Twiss, 1977). If the grain size were, in addition to flow stress, controlled by temperature (e.g. De Bresser et al., 2001), the effect will not cause a difference in observed grain sizes because it is extremely unlikely that a temperature gradient exists between the mylonite and ultramylonite.

The local quartz grain size decrease is observed at sites of initial K-feldspar precipitation (Figs. 11c, 12a and 14a). Second phases like K-feldspar or biotite are known to impede grain boundary migration and form pinning microstructures (Jessell, 1987; Olgaard and Evans, 1988; Song and Ree, 2007). Consequently, pinning locally arrests the grain size at the approximate size of subgrains by impeding grain boundary migration while subgrain rotation still operates as a grain size reduction process (Fig. 16a,b). Thus, by nucleation of second phases in dilatant sites and by suppressing grain boundary migration, phase separation and grain size reduction are linked processes and directly connected to dynamic recrystallization and cavitation.

5.3.2. Solution transfer and phase boundary migration

Dissolution, diffusion, and precipitation are considered to be sequential processes during diffusion creep of geologic materials under low to high grade conditions (Boullier and Gueguen, 1975;

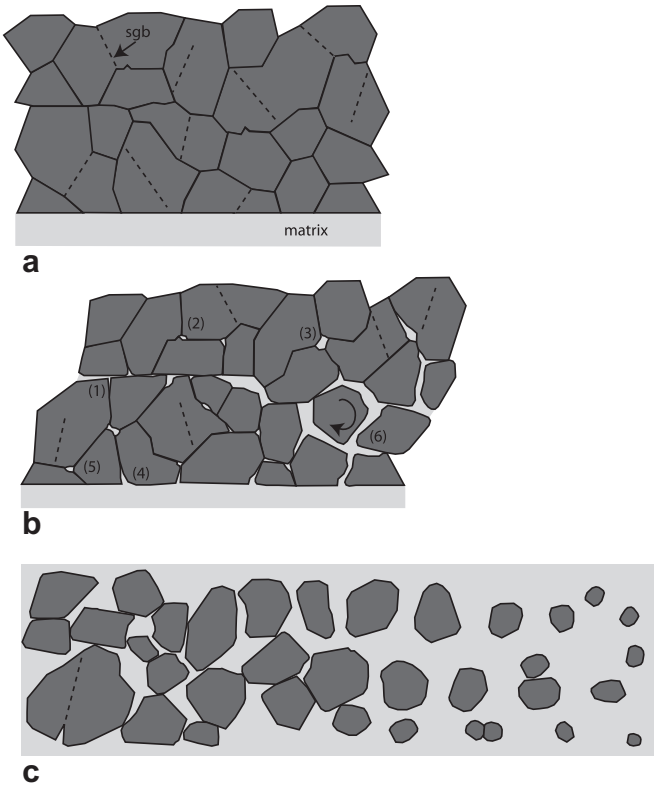

Fig. 16. Schematic model of the aggregate disintegration and grain size reduction. (a) Quartz aggregate undergoing dislocation creep with subgrain rotation and grain boundary migration. The subgrain size is smaller than the dynamically recrystallized grain size as grain boundary migration is associated with a grain size increase. As soon as subgrain boundaries (sgb) become grain boundaries they start to migrate. (b) Initial precipitation of K-feldspar in dilatant sites along aligned grain boundaries (1), asperities (2), opening triple/quadruple junctions (3) and matrix–grain boundary junctions leads to pinning of grain boundaries (5). Coalescence of precipitate filled sites is associated with grain rotation, grain boundary sliding and phase boundary migration. (c) The aggregate is disintegrated, no dynamic recrystallization is possible and further grain size reduction occurs by dissolution–precipitation.

Paterson, 1995; Wintsch and Yi, 2002). Dissolution and precipitation in the Gran Paradiso shear zones are best indicated by several individual microstructures (Fig. 14c–f). The most prominent microstructures are plagioclase grains that protrude into quartz, and the frequent bulging of K-feldspar into quartz (both processes can be termed phase boundary migration). Some geometries of initial quartz grain boundary separations in the fin-shaped structures filled by K-feldspar also suggest a replacement of quartz, especially when they form along subgrain boundaries or directly inside intact grains (Fig. 12b). Phase boundary migration has been reported in high grade and greenschist facies mylonites between quartz and feldspar without an associated grain size decrease (Gower and Simpson, 1992; Stünitz and Fitz Gerald, 1993). Similar microstructures showing a high phase boundary mobility have been interpreted to result from material transport during diffusion creep in greenschist and amphibolite facies mylonites (e.g. Behrmann and Mainprice, 1987), in experimentally deformed harzburgite (Sundberg and Cooper, 2008), and in theoretical modeling (Wheeler, 1992). In the absence of better microstructural criteria, phase boundary migration is one indicator to infer dissolution and precipitation in the Gran Paradiso mylonites and ultramylonites.

The individual size of quartz grains in advanced stages of phase mixing is negatively correlated with the distance between grains which are separated by K-feldspar. In a single layer the average grain size decrease correlates with a relative quartz content decrease, as grains are separated parallel to the foliation and diluted by other phases (Fig. 15c). This is taken as an indicator that the grain size continues to decrease during the extension of the polymineralic aggregate. As dynamic recrystallization does not cause this grain size decrease, dissolution is the most likely explanation (Fig. 16c).

We measure a constant quartz content in the mylonite and the ultramylonite (Fig. 8). These results of the quartz volume fraction agree perfectly with those of LeGoff and Ballevre (1990), who calculated 30.43% qtz for the undeformed Gran Paradiso metagranodiorite and gave a modal quartz content (probably obtained by point counting) of 25% for the magmatic relics. Menegon et al. (2006) report a bulk content of 27% quartz in the protomylonite/mylonite estimated by area measurements on thin sections. Thus, the quartz content is the same in the undeformed rock, the mylonite, and the ultramylonite, independent on the scale of observation and the grain or aggregate size. Chemically there is no significant change in bulk rock composition through the transition from proto to mylonite (LeGoff and Ballevre, 1990; Menegon et al., 2006).

Therefore, quartz dissolution must be accompanied by precipitation near the sites of dissolution (probably on the micron to mm scale). However, there are only few direct indications for quartz precipitation apart from the myrmekite-related quartz (Menegon et al., 2006). During stress induced myrmekite formation, dissolution and precipitation may occur simultaneously at high stress, and low stress sites, respectively (Simpson and Wintsch, 1989). Compare Fig. 11e where K-feldspar precipitates only a few microns away from the myrmekite forming reaction sites at relic K-feldspar clasts. Direct evidence of quartz precipitation in Gran Paradiso mylonites is also found in rare boudinaged garnet, where quartz grows together with biotite and white mica in the necks.

The volume of dissolved quartz in the ultramylonite (as evidenced from the grains size reduction) is at least 75% (conservatively assuming a size reduction from 28 μm to 19 μm, see Fig. 6b,c). Since the total quartz content in the ultramylonite is still 30%, a large fraction of the very fine-grained quartz in the ultramylonite must consist of newly formed grains.

5.3.3. Post-kinematic grain growth

As an alternative to the proposed processes of grain size reduction, annealing could also account for the difference in grain size between the phase mixture and the monomineralic quartz aggregates. Grain growth in the ultramylonite could be impeded by pinning while grains in the monomineralic quartz aggregates could experience substantial growth. However, we do not think that substantial post-kinematic grain growth took place, for the following reasons: 1) Grains in the monomineralic aggregates show anisotropic shape preferred orientations (Figs. 4b, 6e and 7a) consistent with the imposed kinematic framework and the recrystallization mechanism (e.g. Schmid et al., 1987). 2) In the weakly deformed mylonite, a smaller, dynamically recrystallized grain size is preserved locally in quartz aggregates at sites adjacent to large K-feldspar porphyroclasts. This is interpreted to result from stress concentrations. If post-kinematic grain growth would have affected the Gran Paradiso mylonites, these highly stressed grains should have disappeared first (Heilbronner and Tullis, 2002).

Straight boundary segments and equilibrium angles in quartz microstructures are usually related to annealing. However, based on the above-mentioned arguments, a substantial grain size increase due to post-kinematic grain growth in the Gran Paradiso mylonites is unlikely. The observed microstructure is more likely related to a high grain boundary migration rate.

5.4. Origin of the cavitation in quartz aggregates

In quartz aggregates, the K-feldspar and biotite precipitate distribution is heterogeneous at the grain scale but often homogeneous at the aggregate scale (e.g. Figs. 11c,d and 15a). This indicates that the dilatancy is generated during rather homogenous flow of the quartz aggregate and not locally by external perturbations. The presence of precipitates at triple junctions, dilatant grain boundaries and aligned grain boundaries is interpreted to result from cavitation caused by grain boundary sliding (Fig. 16b). Grain boundary sliding commonly occurs during dislocation creep, although to a considerably lesser degree than during diffusion creep, and it is the primary process, which may lead to cavitation (e.g. Crossman and Ashby, 1975; Pilling and Ridley, 1988; Langdon, 1994; Kassner and Hayes, 2003). Cavitation commonly occurs at high angles to the stretching direction (Pilling and Ridley, 1988; Langdon, 1994). Accommodating mechanisms of relative grain movements past asperities during grain boundary sliding are grain boundary diffusion or solution transfer (Ashby and Verrall, 1973) though dislocation movement has also been suggested (Crossman and Ashby, 1975; Gifkins, 1976; Zhao et al., 2009). The presence of chemically different phases – K-feldspar and biotite – in dilatant sites, is interpreted as a process where the local shape accommodation of quartz during crystal plastic deformation was not achieved at a sufficiently high rate, so that cavitation, immediately filled by precipitation of other minerals, has taken place. It should be noted that such a cavitation process can only be inferred if unlike phases precipitate in dilatant sites – precipitation of the same phases is likely to produce overgrowths on existing grains and will not reveal the dilatancy unless associated with chemical changes.

The quartz CPO with a strong peripheral single maximum and prism-parallel subgrain boundaries suggest that basal <a> is the single dominant slip system (Fig. 7a,b). The von Mises criterion (von Mises, 1928) requires 5 independent slip systems in a polycrystal for homogeneous deformation. Fewer slip systems are required if relaxed constraints or recrystallization is introduced (cross-slip or climb of dislocations) (Groves and Kelly, 1969; Honnef and Mecking, 1978). Heterogeneous deformation caused by a limited number of slip systems calls for some process to maintain strain compatibility. Possible accommodating processes are for example diffusive mass transfer or grain boundary migration (Khayutin, 1974; Means and Jessell, 1986). Therefore, grain boundary precipitates may indicate heterogeneous deformation which can result from the activity of the limited number of slip systems in a deforming phase. Grain boundary sliding may arise from heterogeneous deformation and may also cause cavitation instead of accommodating it (Langdon, 1994; Zhang et al., 1996). Small amounts of grain boundary sliding are capable to accommodate heterogeneous strain at the grain scale and in that case do not weaken the CPO of a polycrystalline aggregate deforming with a single slip system (Zhang et al., 1994). In metals the contribution of grain boundary sliding to the total strain during dislocation creep is reported to remain relatively small, probably <15% (Kottada and Chokshi, 2007).

5.5. Shear zone localization

Shear zones tend to localize either by an intrinsic instability (Poirier, 1980) like, e.g. strain rate softening, or by an external inhomogeneity such as a precursor structure (e.g. Segall and Pollard, 1983). In the studied Gran Paradiso shear zones, the existence of a brittle precursor structure was inferred based on the macroscopic shear zone distribution and orientation resembling joint orientations in the same rock (Menegon and Pennacchioni, 2010). From the microstructures this inference can neither be confirmed nor rejected, but additional information is obtained based on microstructural observations: The quartz grain size and thus the flow stress is constant across the mylonite. The switch in deformation mechanism and possible weakening of the rock occurs toward the shear zone center caused by the grain size reduction and phase mixing, especially in thinned quartz layers. The thinning of quartz layers is a progressive strain feature, so that it must have occurred subsequent to initial deformation increments. From these observations, it is clear that the shear zone has narrowed over the deformation history (Hull, 1988; Means, 1995). Thus, if the shear zones are initiated by brittle precursor structures, the rock volume affected by the "precursor effect" (e.g. water infiltration) must have comprised the whole width of the current shear zone. We observe an overprint of strain-dependent structures and therefore the widening of a narrow, crack-like shear zone after its initiation is very unlikely. One possibility for an effect of a precursor crack may be microcracking of the rock volume adjacent to the main crack and aqueous fluid infiltration, causing weakening effects by enhancing transport and reaction rates.

6. Conclusions

From microstructural observations along a strain gradient across a 5 cm wide shear zone the following conclusions can be drawn:

1. In the mylonite, the quartz aggregates (up to 6 mm diameter) deform predominantly by dislocation creep maintaining a dynamically stable grain size of $\mu_V = 110$ μm while the polymineralic fine-grained matrix ($\mu_V \sim 15$ μm) deforms by diffusion creep.
2. In the ultramylonite ($\mu_V \sim 15$–25 μm) only one rheological phase (homogeneous mixture of qtz–kfs–plg–bt) is present; deformation is by diffusion creep.
3. In the mylonite and the ultramylonite, quartz is the phase with the highest viscosity.
4. The texture and microstructure of the quartz aggregates is characteristic for dislocation creep with subgrain rotation and grain boundary migration recrystallization. With the onset of diffusion creep in the ultramylonite, the surface ODF changes from a monoclinic to an orthorhombic symmetry and the CPO is randomized.
5. Failure to deform compatibly with the imposed kinematic framework of the matrix (only basal <a> slip system active), leads to a disintegration of the quartz aggregates by nucleation of K-feldspar (and occasional biotite) along dilatant grain boundaries and triple junctions oriented at high angles to the stretching direction (Fig. 16). From the rim to the center of the quartz aggregates, the deformation mechanism changes from dislocation creep to diffusion creep with grain boundary sliding and cavitation with simultaneous precipitation of second phases (Fig. 16).
6. With the precipitation of K-feldspar and biotite, the grain boundaries in the quartz aggregates (now effectively phase boundaries) are pinned and grain boundary migration is suppressed, causing a local decrease in grain size during dynamic recrystallization from $\mu_V \sim 110$ μm–60 μm. The decreased grain size is approximately equal to the subgrain size.
7. Grain size is further reduced during and after the disintegration of the quartz aggregates from $\mu_V \sim 60$ μm–25 μm such that in the ultramylonite, the grain size of quartz approaches that of the matrix plagioclase and K-feldspar. Dissolution and phase boundary migration contribute to the grain size reduction.
8. The total volume fraction of quartz ($30 \pm 1.5\%$) is constant from the undeformed protolith to the most highly deformed ultramylonite. Dissolution of quartz (leading to the above mentioned grain size comminution) requires that quartz precipitation must take place within the ultramylonite.

9. During diffusion creep of the polymineralic mixture, the surface fabric of K-feldspar and plagioclase is strengthened which indicates grain boundary alignment, impeded grain growth and K-feldspar precipitation adjacent to quartz grains.

Acknowledgments

Luca Menegon and Giorgio Pennacchioni are thanked for introducing RK to the field area and outcrops in the Gran Paradiso and stimulating discussions. Marco Herwegh is kindly thanked for providing access to and help with the EBSD facility at the University of Bern. Willy Tschudin has prepared excellent thin sections. SEM images were taken at the Center of Microscopy, University Basel. The study was founded by the Swiss National Fond grants NF200020 – 108082 and NF200020-119878.

References

Ashby, M., Verrall, R., 1973. Diffusion-accommodated flow and superplasticity. Acta Metallurgica 21 (2), 149–163.
Ayensu, A., Langdon, T., 1996. The inter-relationship between grain boundary sliding and cavitation during creep of polycrystalline copper. Metallurgical and Materials Transactions A – Physical Metallurgy and Materials Science 27 (4), 901–907.
Baker, D., Wenk, H., 1972. Preferred orientation in a low-symmetry quartz mylonite. Journal of Geology 80 (1), 80–81.
Barreiro, J.G., Lonardelli, I., Wenk, H.R., Dresen, G., Rybacki, E., Ren, Y., Tome, C.N., 2007. Preferred orientation of anorthite deformed experimentally in newtonian creep. Earth and Planetary Science Letters 264 (1–2), 188–207.
Behrmann, J., 1985. Crystal plasticity and superplasticity in quartzite – a natural example. Tectonophysics 115 (1–2), 101–129.
Behrmann, J., Mainprice, D., 1987. Deformation mechanisms in a high-temperature quartz feldspar mylonite – evidence for superplastic flow in the lower continental-crust. Tectonophysics 140 (2–4), 297–305.
Bestmann, M., Prior, D., Veltkamp, K., 2004. Development of single-crystal sigma-shaped quartz porphyroclasts by dissolution–precipitation creep in a calcite marble shear zone. Journal of Structural Geology 26 (5), 869–883.
Bons, P.D., Urai, J., 1992. Syndeformational grain-growth – microstructures and kinetics. Journal of Structural Geology 14 (8–9), 1101–1109.
Bons, P.D., den Brok, B., 2000. Crystallographic preferred orientation development by dissolution-precipitation creep. Journal of Structural Geology 22 (11–12), 1713–1722.
Boullier, A., Gueguen, Y., 1975. SP-mylonites – origin of some mylonites by superplastic flow. Contributions to Mineralogy and Petrology 50 (2), 93–104.
Brouwer, F., Vissers, R., Lamb, W., 2002. Structure and metamorphism of the Gran Paradiso massif, western Alps, Italy. Contributions to Mineralogy and Petrology 143 (4), 450–470.
Callegari, E., Compagnoni, R., Piaz, G.D., 1969. Relitti di strutture intrusive erciniche e scisti a sillimanie nel Massicio del Gran Paradiso. Boll Soc Geol Ital 88, 59–69.
Crossman, F., Ashby, M., 1975. Nonuniform flow of polycrystals by grain-boundary sliding accommodated by power-law creep. Acta Metallurgica 23 (4), 425–440.
De Bresser, J., Ter Heege, J., Spiers, C., 2001. Grain size reduction by dynamic recrystallization: can it result in major rheological weakening? International Journal of Earth Sciences 90 (1), 28–45.
De Ronde, A., Stünitz, H., Tullis, J., Heilbronner, R., 2005. Reaction-induced weakening of plagioclase-olivine composites. Tectonophysics 409 (1–4), 85–106.
Drury, M.R., Humphreys, F., 1988. Microstructural shear criteria associated with grain-boundary sliding during ductile deformation. Journal of Structural Geology 10 (1), 83–89.
Edington, J., Melton, K., Cutler, C., 1976. Superplasticity. Progress in Materials Science 21 (2), 63–170.
Fliervoet, T., White, S., 1995. Quartz deformation in a very fine-grained quartzo-feldspathic mylonite – a lack of evidence for dominant grain-boundary sliding deformation. Journal of Structural Geology 17 (8), 1095–1109.
Fliervoet, T., White, S., Drury, M., 1997. Evidence for dominant grain-boundary sliding deformation in greenschist- and amphibolite-grade polymineralic ultramylonites from the Redbank Deformed Zone, Central Australia. Journal of Structural Geology 19 (12), 1495–1520.
Fusseis, F., Regenauer-Lieb, K., Liu, J., Hough, R.M., De Carlo, F., 2009. Creep cavitation can establish a dynamic granular fluid pump in ductile shear zones. Nature 459 (7249), 974–977.
Fynn, G.W., Powell, W.J.A., 1979. The Cutting and Polishing of Electro-optic Materials. Adam Hilger, Bristol, Eng.
Fitz Gerald, J., Stünitz, H., 1993. Deformation of granitoids at low metamorphic grade 1. Reactions and grain-size reduction. Tectonophysics 221 (3–4), 269–297.
Gifkins, R., 1976. Grain-boundary sliding and its accommodation during creep and superplasticity. Metallurgical Transactions A – Physical Metallurgy and Materials Science 7 (8), 1225–1232.
Goetze, C., Kohlstedt, D., 1973. Laboratory study of dislocation climb and diffusion in olivine. Journal of Geophysical Research 78 (26), 5961–5971.
Goldsby, D., Kohlstedt, D., 2001. Superplastic deformation of ice: experimental observations. Journal of Geophysical Research – Solid Earth 106 (B6), 11017–11030.
Gower, R., Simpson, C., 1992. Phase-boundary mobility in naturally deformed, high-grade quartzo-feldspathic rocks – evidence for diffusional creep. Journal of Structural Geology 14 (3), 301–313.
Groves, G., Kelly, A., 1969. Change of shape due to dislocation climb. Philosophical Magazine 19 (161), 977–986.
Guillope, M., Poirier, J.P., 1979. Dynamic recrystallization during creep of single-crystalline halite – experimental-study. Journal of Geophysical Research 84 (NB10), 5557–5567.
Heilbronner, R., Bruhn, D., 1998. The influence of three-dimensional grain size distributions on the rheology of polyphase rocks. Journal of Structural Geology 20 (6), 695–705.
Heilbronner, R., Keulen, N., 2006. Grain size and grain shape analysis of fault rocks. Tectonophysics 427 (1–4), 199–216.
Heilbronner, R., Tullis, J., 2002. The effect of static annealing on microstructures and crystallographic preferred orientations of quartzites experimentally deformed in axial compression and shear. In: De Mehr, S., Drury, M.R., De Bresser, H.J.P., Pennock, G.M. (Eds.), Deformation Mechanisms, Rheology and Tectonics: Current Status and Future Perspectives. Geological Society, London, Special Publications. 200, pp. 191–218.
Herwegh, M., Jenni, A., 2001. Granular flow in polymineralic rocks bearing sheet silicates: new evidence from natural examples. Tectonophysics 332 (3), 309–320.
Hielscher, R., Schaeben, H., 2008. A novel pole figure inversion method: specification of the mtex algorithm. Journal of Applied Crystallography 41, 1024–1037.
Hippertt, J., 1994. Microstructures and *c*-axis fabrics indicative of quartz dissolution in sheared quartzites and phyllonites. Tectonophysics 229 (3–4), 141–163.
Hirth, G., Tullis, J., 1992. Dislocation creep regimes in quartz aggregates. Journal of Structural Geology 14 (2), 145–159.
Holyoke III, C.W., Tullis, J., 2006. Mechanisms of weak phase interconnection and the effects of phase strength contrast on fabric development. Journal of Structural Geology 28 (4), 621–640.
Honnef, H., Mecking, H., 1978. A method for the determination of the active slip systems and orientation changes during single crystal deformation. In: Gottstein, C., Lücke, K. (Eds.), Proc. 5th Int. Conf. Texture of Materials, vol. 5. Springer–Verlag, Berlin, pp. 262–275.
Hull, J., 1988. Thickness displacement relationships for deformation zones. Journal of Structural Geology 10 (4), 431–435.
Ishii, K., Kanagawa, K., Shigematsu, N., Okudaira, T., 2007. High ductility of K-feldspar and development of granitic banded ultramylonite in the Ryoke metamorphic belt, SW Japan. Journal of Structural Geology 29 (6), 1083–1098.
Jessell, M., 1987. Grain-boundary migration microstructures in a naturally deformed quartzite. Journal of Structural Geology 9 (8), 1007–1014.
Kanagawa, K., Shimano, H., Hiroi, Y., 2008. Mylonitic deformation of gabbro in the lower crust: a case study from the Pankenushi gabbro in the Hidaka metamorphic belt of central Hokkaido, Japan. Journal of Structural Geology 30 (9), 1150–1166.
Kassner, M., Hayes, T., 2003. Creep cavitation in metals. International Journal of Plasticity 19 (10), 1715–1748.
Kenkmann, T., Dresen, G., 2002. Dislocation microstructure and phase distribution in a lower crustal shear zone – an example from the Ivrea-Zone, Italy. International Journal of Earth Sciences 91 (3), 445–458.
Kerrich, R., Allison, I., Barnett, R., Moss, S., Starkey, J., 1980. Microstructural and chemical-transformations accompanying deformation of granite in a shear zone at Mieville, Switzerland – with implications for stress-corrosion cracking and superplastic flow. Contributions to Mineralogy and Petrology 73 (3), 221–242.
Khayutin, S., 1974. Deformation of polycrystals connected with grain-boundaries migration. Fizika Metallov I Metallovedenie 37 (5), 1072–1080.
Knipe, R., Law, R., 1987. The influence of crystallographic orientation and grain-boundary migration on microstructural and textural evolution in an S-C mylonite. Tectonophysics 135 (1–3), 155–169.
Kohlstedt, D., Evans, B., Mackwell, S., 1995. Strength of the lithosphere – constraints imposed by laboratory experiments. Journal of Geophysical Research – Solid Earth 100 (B9), 17587–17602.
Kottada, R.S., Chokshi, A.H., 2007. Grain boundary sliding during diffusion and dislocation creep in a Mg-0.7 pct Al alloy. Metallurgical and Materials Transactions A – Physical Metallurgy and Materials Science 38A (8), 1743–1749.
Kretz, R., 1969. On the spatial distribution of crystals in rocks. Lithos 2 (1), 39–65.
Kronenberg, A., Kirby, S., Pinkston, J., 1990. Basal slip and mechanical anisotropy of biotite. Journal of Geophysical Research – Solid Earth and Planets 95 (B12), 19257–19278.
Kruse, R., Stünitz, H., 1999. Deformation mechanisms and phase distribution in mafic high-temperature mylonites from the Jotun nappe, Southern Norway. Tectonophysics 303 (1–4), 223–249.
Langdon, T., 1994. A unified approach to grain-boundary sliding in creep and superplasticity. Acta Metallurgica Et Materialia 42 (7), 2437–2443.
Le Bayon, B., Pitra, P., Ballevre, M., Bohn, M., 2006. Reconstructing P–T paths during continental collision using multi-stage garnet (Gran Paradiso nappe, Western Alps). Journal of Metamorphic Geology 24 (6), 477–496.
LeGoff, E., Ballevre, M., 1990. Geothermobarometry in albite-garnet orthogneisses – a case-study from the Gran-Paradiso nappe (Western Alps). Lithos 25 (4), 261–280.

Lenze, A., Stoeckhert, B., 2007. Microfabrics of UHP metamorphic granites in the Dora Maira Massif, Western Alps – no evidence of deformation at great depth. Journal of Metamorphic Geology 25 (4), 461–475.
Mackenzie, J.R., Egozcue, J.J., Heilbronner, R., Hielscher, R., Müller, A., Schaeben, H., 2008. Quantifying Rock Fabrics – a Test of Independence of the Spatial Distribution of Crystals. CoDaWork08, Girona. http://hdl.handle.net/10256/719.
Means, W.D., 1995. Shear zones and rock history. Tectonophysics 247 (1–4), 157–160.
Means, W., Jessell, M., 1986. Accommodation migration of grain-boundaries. Tectonophysics 127 (1–2), 67–86.
Mehl, L., Hirth, G., 2008. Plagioclase preferred orientation in layered mylonites: evaluation of flow laws for the lower crust. Journal of Geophysical Research – Solid Earth 113 (B5), B05202.
Menegon, L., 2006. Ductile deformation of granitic rocks: Selected examples from the Western Alps. Ph.D. thesis, Univ. Padova, Dip di Geologia., Paleontologia e Geofisica.
Menegon, L., Pennacchioni, G., 2010. Local shear zone pattern and bulk deformation in the Gran Paradiso metagranite (NW Italian Alps). International Journal of Earth Sciences 99 (8), 1805–1825.
Menegon, L., Pennacchioni, G., Stuenitz, H., 2006. Nucleation and growth of myrmekite during ductile shear deformation in metagranites. Journal of Metamorphic Geology 24 (7), 553–568.
Menegon, L., Pennacchioni, G., Spiess, R., 2008. Dissolution–precipitation creep of k-feldspar in mid-crustal granite mylonites. Journal of Structural Geology 30 (5), 565–579.
Mercier, J., 1980. Magnitude of the continental lithospheric stresses inferred from rheomorphic petrology. Journal of Geophysical Research 85 (NB11), 6293–6303.
von Mises, R., 1928. Mechanics of the ductile form changes of crystals. Zeitschrift fur Angewandte Mathematik und Mechanik 8, 161–185.
Olgaard, D., Evans, B., 1988. Grain-growth in synthetic marbles with added mica and water. Contributions to Mineralogy and Petrology 100 (2), 246–260.
Panozzo, R., 1983. Two-dimensional analysis of shape-fabric using projections of digitized lines in a plane. Tectonophysics 95 (3–4), 279–294.
Panozzo, R., 1984. Two-dimensional strain from the orientation of lines in a plane. Journal of Structural Geology 6 (1–2), 215–221.
Panozzo, R., Hurlimann, H., 1983. A simple method for the quantitative discrimination of convex and convex–concave lines. Microscopica Acta 87 (2), 169–176.
Paterson, M., 1995. A theory for granular flow accommodated by material transfer via an intergranular fluid. Tectonophysics 245 (3–4), 135–151.
Pilling, J., Ridley, N., 1988. Cavitation in superplastic alloys and the effect of hydrostatic-pressure. Res Mechanica 23 (1), 31–63.
Poirier, J., 1980. Shear localization and shear instability in materials in the ductile field. Journal of Structural Geology 2 (1–2), 135–142.
Poirier, J., 1985. Creep of Crystals: High-temperature Deformation Processes in Metals, Ceramics and Minerals. Cambridge Univ Press, Cambridge.
Poirier, J., Guillope, M., 1979. Deformation induced recrystallization of minerals. Bulletin De Mineralogie 102 (2–3), 67–74.
Ree, J., 1994. Grain-boundary sliding and development of grain-boundary openings in experimentally deformed octachloropropane. Journal of Structural Geology 16 (3), 403–418.
Rubie, D., 1983. Reaction-enhanced ductility – the role of solid–solid univariant reactions in deformation of the crust and mantle. Tectonophysics 96 (3–4), 331–352.
Rybacki, E., Wirth, R., Dresen, G., 2008. High-strain creep of feldspar rocks: implications for cavitation and ductile failure in the lower crust. Geophysical Research Letters 35 (4), L04304.
Schmid, S., 1982. Microfabric studies as indicators of deformation mechanisms and flow laws operative in mountain building. In: Hsu, K. (Ed.), Mountain Building Processes. Academic Press, London, pp. 95–110.
Schmid, S., Casey, M., 1986. Complete Fabric Analysis of Some Commonly Observed Quartz *c*-axis Patterns. In: Geophysical Monograph, vol. 36. American Geophysical Union. 263–286.
Schmid, S.M., Panozzo, R., Bauer, S., 1987. Simple shear experiments on calcite rocks – rheology and microfabric. Journal of Structural Geology 9 (5–6), 747–778.
Segall, P., Pollard, D., 1983. Nucleation and growth of strike slip faults in granite. Journal of Geophysical Research 88 (NB1), 555–568.
Simpson, C., Wintsch, R., 1989. Evidence for deformation-induced K-feldspar replacement by myrmekite. Journal of Metamorphic Geology 7 (2), 261–275.
Skemer, P., Katayama, I., Jiang, Z., Karato, S., 2005. The misorientation index: development of a new method for calculating the strength of lattice-preferred orientation. Tectonophysics 411 (1–4), 157–167.
Song, W.J., Ree, J.H., 2007. Effect of mica on the grain size of dynamically recrystallized quartz in a quartz-muscovite mylonite. Journal of Structural Geology 29 (12), 1872–1881.
Stünitz, H., Fitz Gerald, J., 1993. Deformation of granitoids at low metamorphic grade .2. granular flow in albite-rich mylonites. Tectonophysics 221 (3–4), 299–324.
Stallard, A., Shelley, D., 1995. Quartz *c*-axes parallel to stretching directions in very low-grade metamorphic rocks. Tectonophysics 249 (1–2), 31–40.
Stipp, M., Stünitz, H., Heilbronner, R., Schmid, S., 2002. The eastern Tonale fault zone: a 'natural laboratory' for crystal plastic deformation of quartz over a temperature range from 250 to 700 °C. Journal of Structural Geology 24 (12), 1861–1884.
Sundberg, M., Cooper, R.F., 2008. Crystallographic preferred orientation produced by diffusional creep of harzburgite: effects of chemical interactions among phases during plastic flow. Journal of Geophysical Research – Solid Earth 113 (B12), B12208.
Trepied, L., Doukhan, J., Paquet, J., 1980. Subgrain boundaries in quartz – theoretical-analysis and microscopic observations. Physics and Chemistry of Minerals 5 (3), 201–218.
Twiss, R., 1977. Theory and applicability of a recrystallized grain-size paleopiezometer. Pure and Applied Geophysics 115 (1–2), 227–244.
Urai, J., Spiers, C., Zwart, H., Lister, G., 1986. Weakening of rock salt by water during long-term creep. Nature 324 (6097), 554–557.
Wheeler, J., 1992. Importance of pressure solution and coble creep in the deformation of polymineralic rocks. Journal of Geophysical Research – Solid Earth 97 (B4), 4579–4586.
Wheeler, J., 2009. The preservation of seismic anisotropy in the earth's mantle during diffusion creep. Geophysical Journal International 178 (3), 1723–1732.
Wintsch, R., Yi, K., 2002. Dissolution and replacement creep: a significant deformation mechanism in mid-crustal rocks. Journal of Structural Geology 24 (6–7), 1179–1193.
Zhang, Y., Hobbs, B., Jessell, M., 1994. The effect of grain-boundary sliding on fabric development in polycrystalline aggregates. Journal of Structural Geology 16 (9), 1315–1325.
Zhang, Y., Jessell, M.W., Hobbs, B.E., 1996. Experimental and numerical studies of the accommodation of strain incompatibility on the grain scale. Journal of Structural Geology 18 (4), 451–460.
Zhao, Y., ZhongYan, W., Kohlstedt, D.I., 2009. Grain boundary sliding in compressed olivine aggregates. Acta Petrologica Sinica 25 (3), 708–712.